Draft version April 18, 2022
Typeset using LaTeX **twocolumn** style in AASTeX62

arXiv:2204.07465v1 [astro-ph.GA] 15 Apr 2022

The State of the Molecular Gas in Post-Starburst Galaxies

K. Decker French,[1] Adam Smercina,[2] Kate Rowlands,[3,4] Akshat Tripathi,[1] Ann I. Zabludoff,[5] John-David T. Smith,[6] Desika Narayanan,[7] Yujin Yang,[8] Yancy Shirley,[5] and Katey Alatalo[9,4]

[1]*Department of Astronomy, University of Illinois, 1002 W. Green St., Urbana, IL 61801, USA*
[2]*Astronomy Department, University of Washington, Seattle, WA 98195, USA*
[3]*AURA for ESA, Space Telescope Science Institute, 3700 San Martin Drive, Baltimore, MD, USA*
[4]*Department of Physics and Astronomy, Johns Hopkins University, Baltimore, MD 21218, USA*
[5]*Steward Observatory, University of Arizona, 933 N Cherry Ave, Tucson, AZ 85721, USA*
[6]*Ritter Astrophysical Research Center, University of Toledo, Toledo, OH 43606, USA*
[7]*Department of Astronomy, University of Florida, 211 Bryant Space Science Center, Gainesville, FL 32611, USA*
[8]*Korea Astronomy and Space Science Institute, 776 Daedeokdae-ro, Yuseong-gu, Daejeon 34055, Republic of Korea*
[9]*Space Telescope Science Institute, 3700 San Martin Dr., Baltimore, MD 21218, USA*

ABSTRACT

The molecular gas in galaxies traces both the fuel for star formation and the processes that can either enhance or suppress star formation. Observations of the molecular gas state can thus point to when and why galaxies stop forming stars. In this study, we present ALMA observations of the molecular gas in galaxies evolving through the post-starburst phase. These galaxies have low current star formation rates, regardless of the SFR tracer used, yet their optical spectra show evidence for recent bursts of star formation that have ended within the last 600 Myr. We present CO (3–2) observations for three post-starburst galaxies, and dense gas HCN/HCO^+/HNC (1–0) observations for six (four new) post-starburst galaxies. The post-starbursts have low excitation as traced by the CO spectral line energy distribution (SLED) up to CO (3–2), more similar to early-type than starburst galaxies. The low excitation indicates that lower density rather than high temperatures may suppress star formation during the post-starburst phase. One galaxy displays a blueshifted molecular gas outflow traced by CO (3–2). MaNGA observations show that the ionized gas velocity is disturbed relative to the stellar velocity field, with a blueshifted component aligned with the molecular gas outflow, suggestive of a multiphase outflow. Low ratios of HCO^+/CO, indicating low fractions of dense molecular gas relative to the total molecular gas, are seen throughout post-starburst phase, except for the youngest post-starburst galaxy considered here.

1. INTRODUCTION

Multiwavelength observations of galaxies across cosmic time are revealing a detailed picture of how galaxies grow, evolve, and ultimately become quiescent. While some galaxies in the local Universe have gradually ended star formation over many Gyr, others show signs of a sudden end to star formation, having undergone rapid evolution from starbursting to quiescent (e.g., Schawinski et al. 2014). Such post-starburst galaxies display substantial populations of young A stars, yet little emission line flux from HII regions around O or B stars, indicating a recent starburst that has since ended (Dressler & Gunn 1983; Couch & Sharples 1987). Post-starburst galaxies provide evidence for fast evolution, likely driven by recent mergers (Zabludoff et al. 1996; Pawlik et al. 2015; Sazonova et al. 2021). At higher redshifts, large fractions of quiescent galaxies show signs of being post-starburst, suggesting that this process of rapid evolution is more common (Wild et al. 2009; Snyder et al. 2011; Whitaker et al. 2012; Wild et al. 2016; Rowlands et al. 2018; Belli et al. 2019; Wild et al. 2020; D'Eugenio et al. 2020). In order to match the high mass, quiescent end of the galaxy population, simulations must add in feedback from active galactic nuclei (AGN) to limit and ultimately end star formation (e.g., Di Matteo et al. 2005; Croton et al. 2006). Yet the process of how and if AGN feedback operates in its different regimes across galaxy type, and the contribution of stellar feedback, is not well understood.

Galaxies evolving through the post-starburst phase are laboratories for understanding how and when star formation ends, the role of feedback processes, and the connection between the evolution of galaxies and their supermassive black holes (see French 2021 for a recent review). In order to understand the changes in star for-

mation, we must look to the molecular gas properties of evolving galaxies to study the potential fuel for that star formation. Previous work has uncovered high molecular gas fractions traced by CO (1–0) single dish observations in multiple samples of post-starburst galaxies (French et al. 2015; Rowlands et al. 2015; Alatalo et al. 2016), contrary to expectations that these galaxies would already be devoid of gas.

The observation of large CO-traced molecular gas reservoirs remaining in post-starburst galaxies raises the question of why they have become quiescent and what prevents the CO-traced molecular gas from forming stars. If large gas reservoirs exist, but are in a relatively diffuse state, this would explain why star formation is no longer occurring at high rates. In previous work, we presented the non-detection of dense gas tracers in two post-starburst galaxies, with upper limits consistent with the low SFRs of these galaxies, indicating that these galaxies have stopped forming stars due to a lack of dense gas (French et al. 2018a). This absence of detected dense gas raises the new question of what physical properties in the diffuse molecular gas are preventing its collapse into forming stars: Is the gas heated? Is it kinematically disturbed? Is there evidence of energy injection from AGN? In order to address these questions, we require detections (rather than limits) of the dense gas tracers in post-starburst galaxies.

In this work, we aim to explore the molecular gas state of post-starburst galaxies by studying their CO excitation and by using multiple tracers of the dense molecular gas from observations with the Atacama Large Millimeter/submillimeter Array (ALMA). We present observations of CO (3–2) for three post-starburst galaxies with previous CO (1–0) and (2–1) observations, as well as observations of dense gas tracers HCN (1–0), HCO^+ (1–0), and HNC (1–0) for four new post-starburst galaxies, which we combine with the previous sample of two measurements from French et al. (2018b). When needed, we assume a flat cosmology with $h = 0.7$ and $\Omega_m = 0.3$.

2. OBSERVATIONS

2.1. *Sample Selection*

We summarize our targets, their coordinates and redshifts, post-burst ages from French et al. (2018a), and ALMA dataset numbers in Table 1. We select our samples from previous studies of CO-traced molecular gas in post-starburst galaxies. We select two samples of galaxies for observing CO (3–2) (rest-frame $\nu = 345.7960$ GHz) in ALMA band 7 and for observing HCN (1–0) (Hydrogen Cyanide; rest-frame $\nu = 88.6316$ GHz), HCO^+ (1–0) (Formylium; rest-frame $\nu = 89.1885$ GHz), and HNC (1–0) (Hydrogen Isocyanide; rest-frame $\nu = 90.6636$ GHz) in ALMA band 3. The CO (3–2) sample is a subset of the HCN/HCO^+/HNC sample.

For the CO (3–2) observations, we select galaxies from the French et al. (2015) sample with CO (1–0) and CO (2–1) detections, declinations observable with ALMA, and redshifts such that the CO (3–2) line is not in regions of high atmospheric absorption. Of the sample of four proposed galaxies, three were observed. Following the naming convention from French et al. (2015), these are H02, H03, and S02.

For the HCN (1–0), HCO^+ (1–0), and HNC (1–0) observations, we select galaxies from French et al. (2015) as well as from the sample of younger post-starburst galaxies from Rowlands et al. (2015). We require the galaxies to have declinations observable with ALMA and redshifts low enough to observe HCN (1–0) before it redshifts out of ALMA Band 3 ($z \lesssim 0.06$). We select galaxies to span the full range of post-starburst age. The inclusion of two galaxies from the Rowlands et al. (2015) sample allows for a wider post-starburst age baseline for this sample. The galaxies R02 and R05 are the second and fifth galaxies in the Rowlands et al. (2015) sample, respectively. From the French et al. (2015) sample, the galaxies H02 and S05 were previously observed with ALMA in various dense gas tracers, as reported in French et al. (2018b). We add an additional two galaxies from this sample: H03 and S02, for a total sample of six post-starburst galaxies with dense gas line measurements HCN (1–0), HCO^+ (1–0), and HNC (1–0).

2.2. *ALMA Observations*

Observations of CO (3–2) for three post-starburst galaxies were taken during Cycle 5 (program 2017.1.00930, PI French). We use the Band 7 receiver and place the redshifted CO (3–2) line in a 1875 MHz wide spectral window with 3840 channels of width 1129 kHz. This corresponds to roughly 1700 km/s with channels of width 1 km/s for our objects. The requested spatial resolution was chosen to be $\sim$ 0.3 arcsec, in order to obtain $\sim$ 9 resolution elements per galaxy, assuming the galaxies had similar size to the CO (2–1) measurements of a partially-overlapping sample from Smercina et al. (2021). The data were pipeline calibrated using the CASA pipeline indicated in Table 2. Briggs weighting was used with the robust values chosen to best match the requested beam size and sensitivity.

Observations of several dense gas tracers were taken of four post-starburst galaxies during Cycles 5 and 6 (programs 2017.1.00935 and 2018.1.00948, PI French). We use the Band 3 receiver and three spectral windows to observe HCN (1–0), HCO^+ (1–0), and HNC (1–0). We use wide spectral windows ($\sim 1600 - 6600$ km/s), de-

pending on the closeness of the lines to the edges of the Band 3 frequency range, and channel widths ~ 2 km/s. The requested spatial resolution was chosen to be 1 arcsecond, in order to match the total spatial extent of the dense gas emission. This resolution scale is larger than the typical size of dense gas emitting clumps, which we do not expect to measure individually. The data were pipeline calibrated using the CASA pipeline indicated in Table 2. Imaging parameters are chosen to best match the requested sensitivity and beam size. For the cases in which no lines are detected (HNC in R05 and all lines in S02), we manually re-image the data using updated continuum regions and natural weighting (robust = 2), but are unable to detect any additional emission. We also re-imaged these datasets using a UV taper of 3 arcseconds and are still unable to detect any additional emission. Two of the datasets (H03 and R02) were manually re-imaged by the ALMA pipeline scientists.

Moment maps and extracted spectra for the both datasets are shown in Appendix A. We extract spectra from a 1.5 arcsec radius centered on the moment 0 map centroid. We integrate the flux density between $\pm 3\sigma_{gauss}$ from the CO (1–0) line measurements in French et al. (2015) and Rowlands et al. (2015). The continuum regions outside of the line regions are used to determine the uncertainty on the flux measurements. The integrated line fluxes are shown in Table 3. In cases where the signal to noise ratio is less than 3, we provide a 3σ upper limit on the possible line flux.

2.3. *Archival Data*

We use Hα-based star formation rates (SFRs) for the post-starburst galaxies from French et al. (2015) and Rowlands et al. (2015) as this measurement is the least biased and most available SFR for our post-starburst sample. The Hα fluxes are from the SDSS (Strauss et al. 2002) MPA-JHU `galSpec` catalogs (Brinchmann et al. 2004; Tremonti et al. 2004), and have been corrected for extinction using the Balmer decrement. For the two Rowlands et al. (2015) galaxies (R02, R05), the SFRs are additionally corrected for the contribution from AGN contamination using the method from Wild et al. (2010). We correct for aperture bias using the `galSpec` SFR aperture bias corrections. The impact of using different SFR indicators is discussed in S4.1. For the sample of post-starburst galaxies with both Hα observations and *Spitzer* [NeII] 12.8μm and [NeIII] 15.6μm observations, we find no evidence that the Hα observations are missing star formation due to dust obscuration. If there was significant dust obscuration for this sample, we would expect to see Ne-based SFRs systematically above the Hα-based SFRs. Instead, we see no systematic shift between the two tracers. Thus, we use Hα-based SFRs throughout the main body of this work, and present the results if infrared tracers are used in Appendix B.

3. RESULTS

3.1. *Gas Excitation*

Observations of multiple J CO lines trace the excitation of the molecular gas; the shape of the CO spectral line energy density (SLED) depends on the density, kinetic temperature, and observed column density of the gas (Weiß et al. 2007; Carilli & Walter 2013; Narayanan & Krumholz 2014; Bournaud et al. 2015; Kamenetzky et al. 2018). We combine the CO (3–2) measurements of three post-starburst galaxies from this survey with CO (2–1) and CO (1–0) measurements from the IRAM 30m from French et al. (2015). Resolved studies of CO (2–1) with ALMA of a subset of these galaxies from Smercina et al. (2021) show that the molecular gas in post-starburst galaxies is compact, on $\lesssim 1$ arcsec scales, such that the ALMA observations are not resolving out extended flux, and the single dish measurements are comparable to the ALMA measurements. We compare the ALMA CO(2–1) flux measurements from Smercina et al. (2021) to the IRAM 30m measurements from French et al. (2015) to estimate the uncertainties introduced from combining the measurements. For H02 and H03, the ALMA and IRAM CO (2–1) measurements differ by $\sim 37\%$. For H02, the IRAM flux is larger than the ALMA flux; for H03 the ALMA flux is larger than the IRAM flux. We do not have ALMA CO (2–1) measurements for S02, so we assume it will have a similar uncertainty. These errorbars are reflected in Figure 1.

We compare the CO SLEDs of the three post-starburst galaxies with CO (3–2) measurements with other galaxy samples in Figure 1. The post-starburst galaxies have low CO excitation, consistent with the population of early type galaxies (Crocker et al. 2012; Bayet et al. 2013), slightly below the population of star forming galaxies (Leroy et al. 2021), and below most of the LIRGs (Papadopoulos et al. 2012). Even considering the uncertainties from combining ALMA and IRAM measurements, the post-starburst galaxies have low excitation.

Observations of CO (1–0) and CO (2–1) in post-starburst galaxies show low star formation efficiencies (SFEs), SFE $\propto$ SFR/$L'_{\rm CO}$ (French et al. 2015; Rowlands et al. 2015; Alatalo et al. 2016; Smercina et al. 2018; Smercina et al. 2021). The excitation of the CO-traced gas can be used to distinguish between two possible mechanisms that could suppress star formation in the molecular gas, leading to these low SFEs. The first possibility is high kinetic temperatures in the gas paired

Galaxy	R.A. (deg)	Decl. (deg)	z	Post-burst Age (Myr)	HCN/HCO^+/HNC Dataset	CO (3–2) Dataset
H02	141.580	18.6781	0.0541	201	(2016.1.00881; [1])	2017.1.00930
H03	222.067	17.5517	0.0449	381	2017.1.00935	2017.1.00930
S02	49.2288	-0.0420	0.0231	522	2017.1.00935	2017.1.00930
S05	146.112	4.49912	0.0467	259	(2016.1.00881; [1])	
R02	228.951	20.0224	0.0363	-4	2018.1.00948	
R05	244.398	14.0523	0.0338	10	2018.1.00948	

Table 1. Post-starburst galaxy targets. Names match those in French et al. (2015); Smercina et al. (2018); French et al. (2018b); Smercina et al. (2021). Galaxy coordinates and redshifts are from the SDSS main spectroscopic survey (Strauss et al. 2002). Post-burst ages measure the time since the starburst ended, taken from French et al. (2018a). Galaxies with negative ages are those where the best-fit model is a still-declining burst. [1] French et al. (2018b).

Target	Dataset	Beam size ($''$)	CASA Pipeline	robust
H03 HCO^+ (1–0)	2017.1.00935	1.26 × 1.06	5.1.1-5	0
S02 HCO^+ (1–0)	2017.1.00935	0.97 × 0.88	5.4.0-68	2
R02 HCO^+ (1–0)	2018.1.00948	1.03 × 0.86	5.4.0-68	1
R05 HCO^+ (1–0)	2018.1.00948	1.16 × 0.80	5.4.0-68	2
H02 CO (3–2)	2017.1.00930	0.39 × 0.38	5.1.1-5	0.5
H03 CO (3–2)	2017.1.00930	0.39 × 0.34	5.4.0-68	-0.5
S02 CO (3–2)	2017.1.00930	0.26 × 0.23	5.4.0-68	2

Table 2. ALMA Observations. Beam sizes and robust values for Briggs weighting were chosen to best match the requested beam size and sensitivity.

Galaxy	HCN (1–0) (Jy km/s)	HCO^+ (1–0) (Jy km/s)	HNC (1–0) (Jy km/s)	CO (3–2) (Jy km/s)
H02	< 0.13	< 0.13		18.87 ± 0.55
H03	0.98 ± 0.02	0.32 ± 0.02	0.25 ± 0.02	71.52 ± 0.45
S02	< 0.08	< 0.09	< 0.09	20.17 ± 0.22
S05	< 0.05	< 0.05		
R02	0.21 ± 0.03	0.51 ± 0.03	0.13 ± 0.03	
R05	0.22 ± 0.03	0.51 ± 0.03	< 0.09	

Table 3. Measured Integrated Line Fluxes $S_\nu dv$.

with low gas densities; in this case, we would expect to see high gas excitation throughout the post-starburst phase. High excitation could also arise from both high temperatures and high densities like those in starburst galaxies, but we would expect to see starburst-like SFRs if the densities were also high. The second possibility for why the post-starburst galaxies have low SFE is if the gas densities are low. In this case, we would expect to see low gas excitation, similar to early type galaxies, throughout the post-starburst phase. The observations of the post-starburst excitation presented here favor the second possibility, that the post-starburst galaxies have low densities and temperatures[1]. The low density may explain the low SFEs.

We explore these possibilities more quantitatively by modelling the CO SLEDs with RADEX (van der Tak et al. 2007). RADEX is a non-LTE (non local thermodynamic equilibrium) code that solves for the radiative transfer of a given molecular species, assuming a geometry. Here, we assume a uniform sphere geometry. We use a grid of logarithmically-spaced values in tempera-

[1] These low temperatures are indicative of the state of the CO, but are not sensitive to the large scale motions that appear to increase the velocity dispersion of the gas. Smercina et al. (2021) infer a source of turbulent heating from high velocity dispersions of CO (2–1) observations, yet this does not preclude the low CO excitation observed here.

ture (T; $10-300$ K), density (n; 10^1-10^7 cm^{-3}), and column density of CO (N; $10^{13}-10^{21}$ cm^{-2}), similar to that used by Krips et al. (2011). We generate the expected flux ratios of the CO (1–0), CO (2–1), and CO (3–2) lines for this grid of parameters and compare them to the observed line ratios.

The inferred density and temperature values are highly degenerate unless the full rise and turnover of the CO SLED can be sampled (e.g., Carilli & Walter 2013; Kamenetzky et al. 2018). We visualize these degeneracies by plotting the likelihoods for the temperature, density, and column density of each source in Figure 2. Densities of $\log n \sim 3.4-3.8$ cm^{-3} and temperatures of $T \sim 15-30$ K are favored, although clear degeneracies can be seen between the cases of low density with relatively unconstrained temperature and higher density with low temperature. These values are similar to molecular gas densities and temperatures in early type galaxies (Bayet et al. 2013), which have densities of $\log n \sim 3-4$ cm^{-3} and temperatures of $T \sim 10-70$ K. The post-starburst galaxies have both temperatures and densities less than typical LIRGs. LIRGs have a wide range of densities of $\log n \sim 2.5-6.5$ cm^{-3} and temperatures of $T \sim 30-120$ K (e.g., Greve et al. 2009; Papadopoulos et al. 2012).

We perform additional RADEX modeling of the dense gas tracers HCN (1–0) and HCO$^+$ (1–0) in addition to the CO lines. This analysis is complicated by the need to assume an abundance ratio of either [HCO$^+$/CO] or [HCN/CO]. For both dense gas tracers, we assume an abundance ratio with respect to CO of 10^{-4} (consistent with the range of measurements by Krips et al. 2008; Aalto et al. 2012). Due to the uncertainties in what is affecting the HCO$^+$/HCN ratio (§3.6), we consider each dense gas tracer individually. In Figure 3, we show the parameter likelihood corner plots considering CO (1–0), CO (2–1), CO (3–2) and either HCO$^+$ (1–0) or HCN (1–0) for the two post-starburst galaxies (H03, S02) with both datasets. For S02, neither dense gas tracer is detected, so we assume the dense gas flux ratios are just below the detection threshold. When the HCO$^+$ constraints are included, the best-fit densities are similar, with sharp cutoffs in likelihood above $\log n \sim 4$, the effective excitation density of the dense gas tracers (Shirley 2015).

The cold molecular gas temperatures indicated by the low CO excitation do not preclude the existence of an additional component of warm or hot gas, as the low J CO lines cannot predict the full SLED in the event of a secondary component of high temperature molecular gas. In our RADEX analysis, we have assumed the molecular gas is composed of a single temperature component. However, studies of star-forming and starburst galaxies (e.g., Valentino et al. 2020) have found evidence for multiple components using higher J CO lines than available here. A secondary component of high excitation molecular gas was also found for NGC 1266 by Pellegrini et al. (2013), better fit by shock models than PDR models. The post-starburst galaxies considered here may also have multiple components of molecular gas, which would require additional CO lines to uncover, and may have different filling fractions. Indeed, we expect that such a component exists, as traced by mid-IR H_2 rotational lines (Smercina et al. 2018). The extremely high H_2/TIR ratios observed by Smercina et al. (2018) are indicative of shocks heating a portion of the molecular gas to high temperatures, with a "high-soft" radiation field affecting the dust. By modeling the mass of H_2 using the mid-IR warm H_2 lines (Togi & Smith 2016) and extrapolating down in temperature to the low temperature regime probed by the $J \leq 3$ CO lines, Smercina et al. (2018) find gas masses typically within a factor of $2-4\times$ the mass of cold gas inferred from CO (1–0). The higher temperature gas traced by the mid-IR lines comprises a relatively small fraction of the overall mass. By combining these observations, we conclude that the bulk of the gas by mass remains at temperatures lower than typical LIRGs, while a fraction of the molecular gas is highly excited.

We compare the CO (3–2) / CO (1–0) intensity ratio as a tracer of the molecular gas temperature to the mean interstellar radiation field (ISRF) intensity $\langle U \rangle$ calculated from dust SEDs in Figure 4. The $\langle U \rangle$ is closely coupled to the dust temperature. Smercina et al. (2018) used Draine & Li (2007) models to fit the infrared SEDs of post-starburst galaxies, including the galaxies considered here. We use the best-fit values of the minimum ISRF intensity U_{min} and power law index γ from Smercina et al. (2018) and the conversion to $\langle U \rangle$ from Draine et al. (2007) to calculate $\langle U \rangle = 35.6, 15, 11.7$ for H02, H03, and S02, respectively. Cross matching with the CO SLED data above, we obtain $\langle U \rangle$ measurements for LIRGs from Liu et al. (2021) and for the star forming and early type galaxies from Draine et al. (2007). For normal star forming and star bursting galaxies, the CO excitation is correlated with $\langle U \rangle$. This is consistent with previous work, e.g., Liu et al. (2021) find the CO R52 ratio to be well correlated with $\langle U \rangle$. While the post-starburst galaxies have high $\langle U \rangle$ values similar to the LIRGs, their low CO excitation is more consistent with star forming and early type galaxies. The post-starburst galaxies lie in an unusual region of this parameter space, having high $\langle U \rangle$ values similar to LIRGs, but low CO excitation, indicating the dust and gas temperatures are

not well-coupled. The decoupled dust and gas temperatures stand in contrast to the coupled time evolution observed during the post-starburst phase (Smercina et al. 2018; Li et al. 2019).

3.2. *Spatially-resolved and velocity-resolved observations*

We construct zeroth-, first-, and second- order moment maps for the three post-starburst galaxies with CO (3–2) observations, presented in Appendix A. The CO (3–2) emission for each of the three post-starburst galaxies observed has limited extent relative to the optical emission, consistent with the CO (2–1) results from Smercina et al. (2021). The half-light radius of the CO (3–2) emission for each galaxy is shown in Table 4. The sizes range from 0.38–0.57 arcsec, or 367–400 pc. On average, the CO (3–2) sizes are 6.3× smaller than the r-band sizes from the SDSS imaging. Two galaxies (H02 and H03) have both CO (3–2) and CO (2–1) observations; these galaxies have sizes consistent between the two tracers, although differences would be difficult to determine with these observations, as $> 50\%$ of the flux is contained within a central unresolved beamsize in both tracers for both galaxies. The velocity and velocity dispersion maps are broadly consistent as well. The galaxy S02 has archival MaNGA (Bundy et al. 2015) IFU data. In Figure 5, we compare the CO (3–2) emission to the post-starburst region with high Hδ absorption. The molecular gas is smaller than the extent of the young stellar population traced by the Hδ_A index.

The small CO (3–2) and CO (2–1) sizes imply very high surface densities of molecular gas and residual star formation. Because of the consistency in sizes between the CO (3–2) measurements here and the CO (2–1) sizes measured by Smercina et al. (2021), we assume these sizes in calculating the molecular gas surface density $\Sigma_{\rm H_2}$ from the CO (1–0) luminosities from French et al. (2015). Using the half-light sizes, we calculate the densities as:

$$\Sigma_{\rm H_2} = 0.5 \frac{M_{H_2}}{\pi R_{1/2}^2} \quad (1)$$

$$\Sigma_{\rm SFR} = 0.5 \frac{SFR}{\pi R_{1/2}^2}. \quad (2)$$

We compare our observations to the samples of star-forming galaxies from de los Reyes & Kennicutt (2019) and starbursting galaxies from Kennicutt & De Los Reyes (2021) in Figure 6. We use a CO-to-H_2 conversion factor of 4 $M_\odot$ $(\rm K\,km\,s^{-1}\,pc^2)^{-1}$ for all samples. The post-starburst galaxies have very high molecular gas surface densities, yet they lie below the comparison galaxies, with low star formation rate surface densities for their molecular gas surface densities. The effects of star formation tracer on these results is explored further in §4.1 and Appendix B; we observe qualitatively similar results using infrared tracers instead of the Hα SFR tracers used for the post-starburst galaxies here. Six of the seven galaxies presented in Figure 6 are the sample from Smercina et al. (2021); the addition of the measurement for S02 does not change the interpretation of this result. The values of $\Sigma_{\rm H_2}$ and $\Sigma_{\rm SFR}$ differ slightly from those presented by Smercina et al. (2021) due to the inclusion of the [CII] tracer and a different method for calculating the surface densities. but the qualitative conclusions are consistent. We use the half-light sizes, as these can be more robustly determined than outer sizes like the 95 percentile size used by de los Reyes & Kennicutt (2019) and Kennicutt & De Los Reyes (2021), though we verify that our qualitative conclusions do not change with the use of 95 percentile radii, regardless of SFR tracer.

Galaxy	CO (3–2) size (arcsec)	CO (3–2) size (pc)	r-band R50[a] (arcsec)
H02	0.38	400	1.71
H03	0.41	355	3.17
S02	0.57	267	3.72

Table 4. CO (3–2) Galaxy Half-light Sizes. [a] From the SDSS.

Evidence of rotation is seen in the velocity fields of all three sources, though the peak velocity dispersion values are higher than the peak velocities. These behaviors are consistent with the range in CO (2–1) velocity and velocity dispersion maps seen by Smercina et al. (2021). The high CO(2–1) velocity dispersion and small size measured by Smercina et al. (2021) for H02 and H03, which led them to infer a high turbulent pressure, is also observed here. In the case of one galaxy, S02, we see evidence for a blueshifted outflow, which we explore further in the next section.

3.3. *Blueshifted Outflow*

S02 has a blueshifted component to the south east of the CO (3–2) centroid. We explore the nature of this component further in Figures 7, 8, and 9. A channel map of the CO (3–2) observations is shown in Figure 7, overlaid on the moment 0 map. The blueshifted component at velocities -64 – -108 km $\rm s^{-1}$ is roughly aligned with the rotational axis of the galaxy, but extends to larger radius and does not have a symmetric redshifted component on the northwest side, as we would expect if this component were caused by rotation instead of an outflow.

We fit a series of tilted 3D ring models to S02 using Barolo (Di Teodoro & Fraternali 2015) to model the

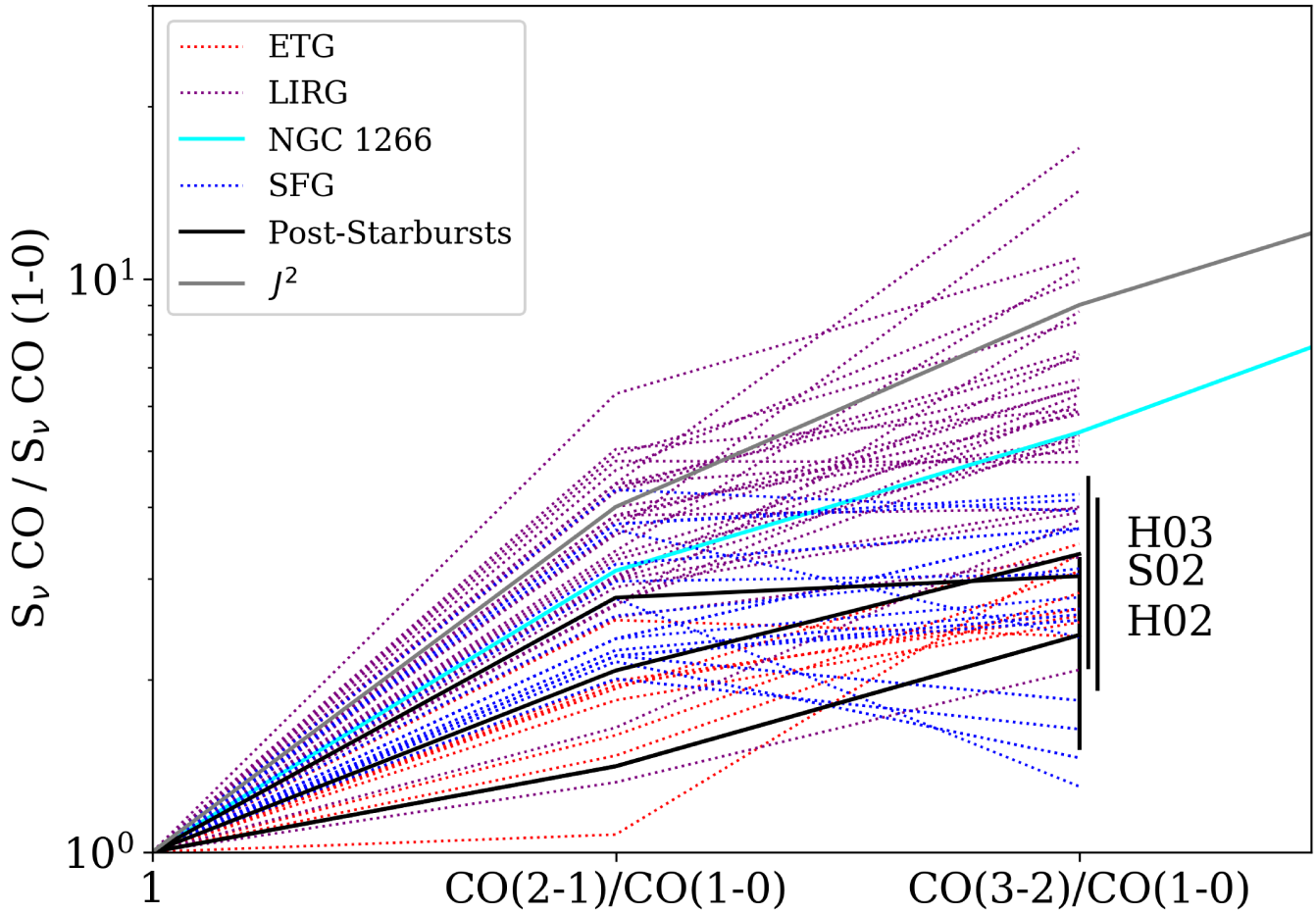

Figure 1. CO Spectral Line Energy Density (CO SLED) for the three post-starburst galaxies observed in CO (3-2) (with data for CO (2-1) and CO (1-0) from French et al. 2015), their likely progenitors (LIRGs[b], Papadopoulos et al. 2012), star forming galaxies (Leroy et al. 2021), and their likely descendants (early type galaxies, Crocker et al. 2012; Bayet et al. 2013). We also include the shocked post-starburst galaxy NGC 1266 (Pellegrini et al. 2013). The post-starburst galaxies presented here have excitation states more similar to the early type galaxies than the LIRGs, with lower excitation than observed for NGC 1266. We observe no trend with age within the post-starburst sample.

[a]Several of the LIRGs have CO SLEDs above the expectation for thermalized gas, likely due to optical depth effects.
[b]Several of the LIRGs have CO SLEDs above the expectation for thermalized gas, likely due to optical depth effects.

kinematics of the molecular gas. The position-velocity diagram of the data and best-fit model are shown in Figure 8. The best-fit kinematic major axis of the molecular gas is consistent with that of the stellar velocity. In the position-velocity diagram, the excess flux in the most blueshifted component at $\sim$ 100 km s^{-1} can be seen, inconsistent with the model.

We compare the CO (3–2) observations for S02 with archival *HST* imaging (PI: Zabludoff, ID 11643) and MaNGA (Bundy et al. 2015) IFU data in Figure 9. The stellar velocity field from MaNGA is aligned with the bulk of the molecular gas velocity. The southeastern component is blueshifted with respect to the surrounding stellar velocity field, indicative of an outflowing component. The ionized gas traced by the optical emission lines[2] is disturbed in morphology with respect to the stellar velocity, with the ionized gas blueshifted by $\sim$ 40 km s^{-1} relative to the stellar velocity field. The blueshifted CO component is aligned with the blueshifted ionized gas region, indicating a multiphase (both ionized and molecular gas) outflow. When we compare the location of this component to the *HST* image, it is aligned with a dust lane. It is unlikely that the dust lane is the source of the abnormal ionized gas velocity field, as the blueshifted ionized gas component extends several arcseconds outside of the dust lane.

[2] The velocities for all optical emission lines are fixed to one another during the fitting process (Westfall et al. 2019).

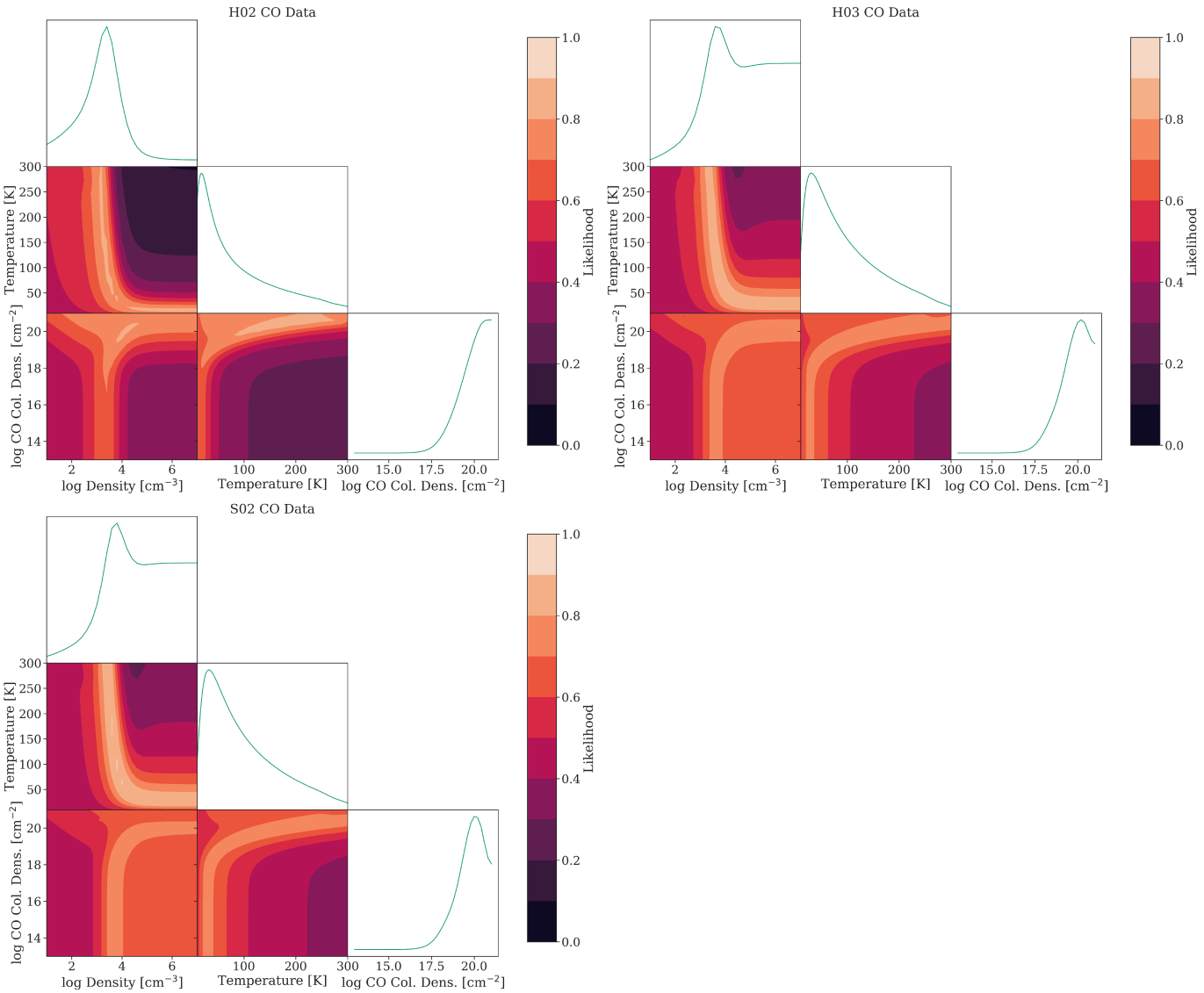

Figure 2. Corner plot of likelihoods of temperature, density, and CO column density comparing RADEX models to our observations of CO (1–0), (2–1), and (3–2) for each galaxy. Line plots show the likelihood marginalized over the other two parameters, and contour plots show the likelihood marginalized over the third parameter to show the degeneracies present between parameters. For each galaxy, the best-fit models favor low densities ($\log n/[\mathrm{cm}^{-3}] \sim 3.4 - 3.8$) and temperatures $T \sim 15 - 30$ K, similar to early type galaxies and lower than typical LIRGs.

Thus, while the blueshifted component is aligned with the stellar velocity field and bulk rotation of the molecular gas, it is more likely to be an outflow than an extension of the molecular gas rotation due to (1) the spatially-distinct morphology of the outflow (see in Figure 7), (2) the asymmetric nature and lack of a counterpart on the northwest side, as evidenced by the excess flux above the best-fit Barolo model (see Figure 8), and (3) the velocity excess over the surrounding stellar velocity field (see Figure 9). The blueshifted component is unlikely to be a parcel of infalling gas from the recent merger, as the smooth stellar velocity field suggests any merger components have already coalesced.

We consider the bulk properties of this component, assuming a distance from the center of the galaxy of 1″(460 pc) and a velocity of 100 km s^{-1}, based on the blueshifted component's position in the channel map and position-velocity diagram. If this component is an outflow, its characteristic timescale τ is 4.5 Myr. The south east component consists of $\sim 15\%$ of the total flux. Scaling the CO (1–0) inferred molecular gas mass from French et al. (2015) by 15%, the expected mass in this outflowing component is $7.3{\times}10^7$ M$_\odot$, and the average outflow rate over the timescale of the outflow is 16 M$_\odot$ yr^{-1}. This is consistent with the (large) range of typical molecular gas depletion rates inferred for the combined

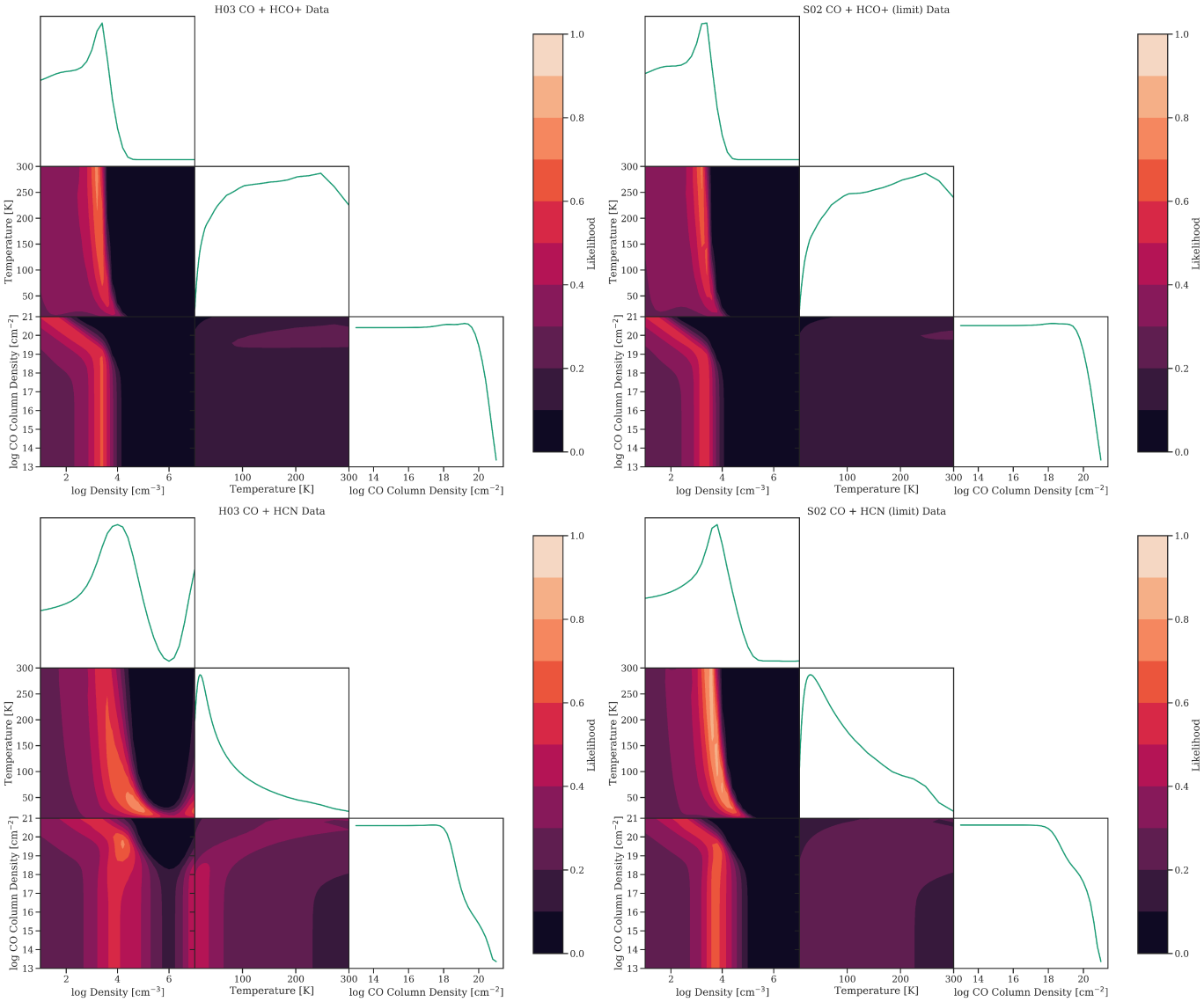

Figure 3. Same as Figure 2, but with the observations of the dense gas tracers (top row: HCO^+ (1–0); bottom row: HCN (1–0)) for the two galaxies with both dense gas measurements and CO (3–2) measurements. We assume an abundance ratio of [HCN]/[CO] = [HCO^+]/[CO] = 10^{-4}, and assume the dense gas flux ratios are just below the detection threshold for the non-detections of galaxy S02. The low ratios of dense molecular gas to total molecular gas inferred from the [HCO^+]/[CO] ratios is also reflected here in the steep dropoff in likelihood in densities $\log n/[\mathrm{cm}^{-3}] > 4$. However, we do not have enough data to constrain the likely abundance ratios, and thus these additional dense gas measurements do not provide useful constraints on the temperature or CO column density.

post-starburst population by French et al. (2018a). The mass traced by the molecular outflow will dominate over the mass in the ionized gas component, as ionized gas outflow rates are typically low $\sim 10^{-2}$ $M_\odot$ yr^{-1} (Baron & Netzer 2019).

In order to determine the likely fate of this outflowing gas, we compare the outflow velocity to the escape velocity at its radius of 1″(460 pc). We use the stellar mass from the SDSS (Strauss et al. 2002; Brinchmann et al. 2004; Tremonti et al. 2004) and the *HST* observations to estimate the stellar mass within this radius to be $M_\star = 2.04 \times 10^9$ $M_\odot$. The escape velocity is thus 195 km s^{-1}. The outflow velocity of $\sim$ 100 km s^{-1} is less than the escape velocity, but given inclination effects, if the angle of the outflow from our line of sight is $> 60°$, may exceed the escape velocity from the center of the galaxy.

The inferred outflow kinetic power using $P = \frac{1}{2} M_{\mathrm{outflow}} v^2/\tau$ is 8×10^{40} erg s^{-1}. The molecular outflow is comparable to those in star-forming galaxies and LINERs, and has less kinetic power than those in luminous AGN (Cicone et al. 2014). Another source of energy

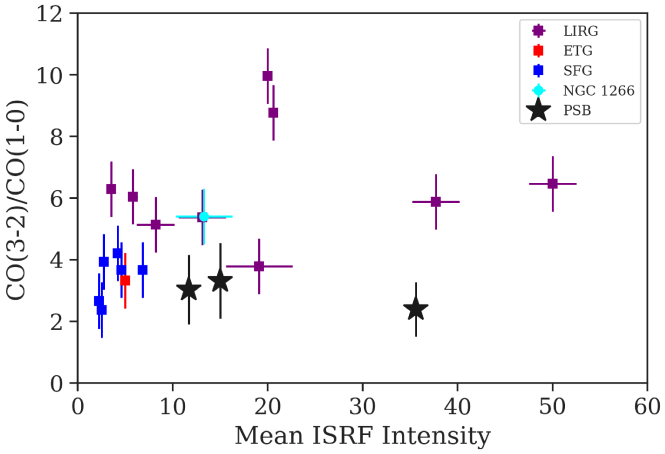

Figure 4. CO (3–2) / CO (1–0) intensity ratio (sensitive to gas temperature) vs. mean interstellar radiation field intensity $\langle U \rangle$ calculated from dust SED fitting (sensitive to dust temperature). Post-starburst galaxy $\langle U \rangle$ is measured from the best-fit parameters in Smercina et al. (2018) using the relation in Draine et al. (2007). LIRG $\langle U \rangle$ measurements are from Liu et al. (2021) and star-forming and early type galaxy measurements are from Draine et al. (2007). CO measurements are as above. While post-starburst galaxies can have high $\langle U \rangle$ values similar to LIRGs, these dust temperatures are not well-coupled to the colder molecular gas.

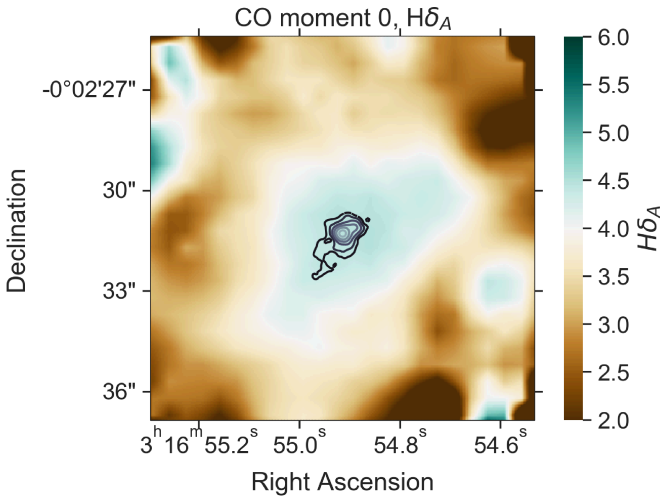

Figure 5. ALMA CO (3–2) observations of S02 (contours) with complementary MaNGA (Bundy et al. 2015) observations (MaNGA plateID 8080-3072) accessed via Marvin (Cherinka et al. 2019). The Hδ_A index traces the young A-star dominated stellar population and indicates the post-starburst regions of the galaxy. The molecular gas region is smaller than the post-starburst region (teal; H$\delta_A \gtrsim 4$).

may be tidal disruption events (TDEs), which occur at higher rates in post-starburst galaxies than normal galaxies (French et al. 2016, 2020). As in Smercina et al. (2021), we consider the energy input of $\sim 10^{51} - 10^{53}$ erg per TDE (Mockler & Ramirez-Ruiz 2021) and a typical TDE rate of 10^{-3} per year per post-starburst galaxy (French et al. 2016), resulting in a total energy source of $\sim 3 \times 10^{40-42}$ erg s^{-1}. The feasibility for energy driving this outflow to come from intermittent AGN/LINER activity or from TDEs will depend heavily on the coupling to the molecular gas in these galaxies.

The MaNGA data for this source also allow us to investigate the nature of the LINER-like emission seen in the SDSS spectrum. Using the MaNGA data to construct a resolved BPT (Baldwin et al. 1981; Kewley et al. 2001; Kauffmann et al. 2003) diagram, most of the galaxy has low emission line fluxes such that the classification is ambiguous, but the spaxels that can be classified are in the LINER part of the BPT diagram (Figure 10). This LINER-like signature extends outside of the nucleus over ~ 5 arcsec (10 spaxels), significantly more than the 2.5 arcsec FWHM of MaNGA's spatial resolution (Law et al. 2016). It is thus more likely to be caused by post-AGB stars (Sarzi et al. 2010; Yan & Blanton 2012) or shocks (Rich et al. 2015) than low luminosity AGN activity. However, if the "ring" like structure is a real feature, it could be an echo of previous nuclear activity $\tau \sim 3000$ years ago.

While this galaxy does not show evidence for ongoing luminous AGN activity, the timescale for AGN to vary is much smaller than the characteristic timescale of this outflow. AGN are observed to change dramatically, turning on and off on timescales $\sim 10^4 - 10^5$ years (Keel et al. 2012; Sartori et al. 2018; Shen 2021). The molecular gas outflow we observe would have been launched 4.5 Myr ago, when the galaxy could have had now-faded AGN activity.

3.4. *Evolution During the Post-Starburst Phase*

The evolution of the molecular gas state during the post-starburst phase can provide more information than comparing the average properties to other classes of galaxies. We found in French et al. (2018a) that the CO-traced molecular gas fraction declined during the post-starburst phase, after 90% of the starburst is complete, with a timescale of ~ 200 Myr. A similar decline has been seen in the CO-traced molecular gas in higher redshift post-starburst galaxies (Bezanson et al. 2021; Suess et al. 2021). The low SFRs during this period of decline cannot be responsible for depleting this gas via consumption or stellar feedback, suggesting that another mechanism like AGN feedback is operating late into the

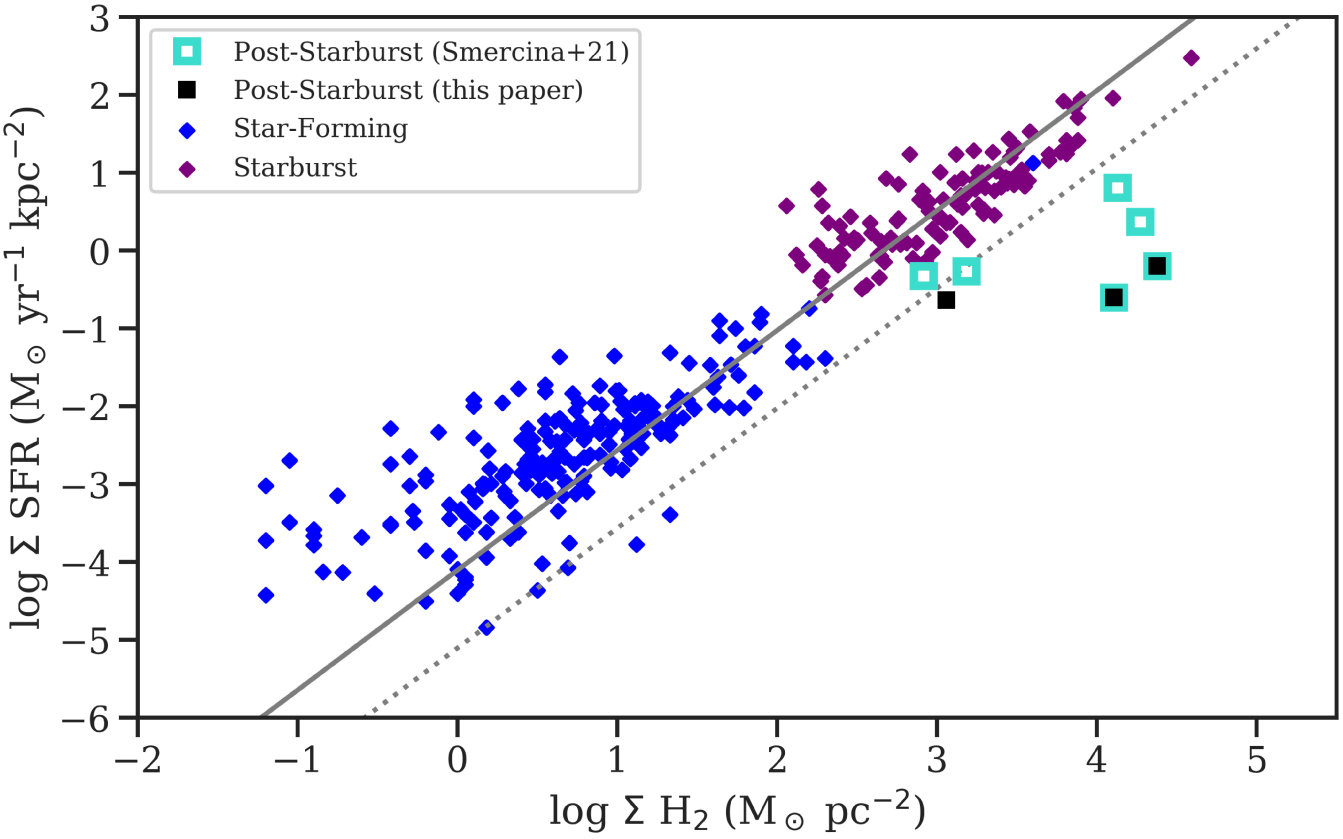

Figure 6. Molecular gas surface density vs. SFR surface density for post-starburst galaxies from this work with CO (3–2) sizes and from Smercina et al. (2021) with CO (2–1) sizes, as well as comparison samples of star-forming galaxies from de los Reyes & Kennicutt (2019) and starbursting galaxies from Kennicutt & De Los Reyes (2021). The best-fit relation from Kennicutt & De Los Reyes (2021) for the total gas density vs. star formation density is plotted in grey, with a dotted line indicating a factor of 10× below the relation. The post-starburst galaxies have very high molecular gas surface densities, yet they lie below the comparison galaxies, with low star formation rate surface densities for their molecular gas surface densities. This result does not depend on the SFR tracer used, see Appendix B and Figure 21.

post-starburst phase. The dust fraction is also observed to decline during the post-starburst phase (Smercina et al. 2018; Li et al. 2019), with a timescale consistent with that of the CO-traced molecular gas (Li et al. 2019). Li et al. (2019) considered the evolution of the star formation efficiency (traced by SFR/(α_{CO} L'_{CO}), finding a rapid decline in SFE during the first 200 Myr of the post-starburst phase, which levels off to a shallower decline in after 200 Myr post-burst. This two-phase evolution in SFE implies a two-phase evolution in SFR and a faster initial timescale of SFR evolution compared to the CO-traced molecular gas.

Such a two-phase evolution in SFR with post-burst age was observed by Rowlands et al. (2015) in both the Hα and FIR-based SFRs. A short $\sim$ 30 Myr decline was followed by a plateau of $\sim$ 400 Myr. The overall timescale for the SFR to drop was $\sim 200 - 300$ Myr.

We illustrate the evolution of the specific SFR (sSFR) and various tracers of the molecular gas in Figure 11. We plot the sSFR traced by Hα for the three post-starburst samples from French et al. (2015); Rowlands et al. (2015); Alatalo et al. (2016). Post-burst ages are from French et al. (2018a) and measure the time elapsed since the end of the recent starburst (the age since 90% of the stars were formed[3]). The sSFR trend qualitatively appears to follow that expected from Rowlands et al. (2015) and Li et al. (2019), with a rapid initial decline that levels off at later times. Rowlands et al. (2015) observed a third phase of more rapid decline after 400 Myr in the Hα SFRs, which we do not observe here. This may be driven by differing treatments of the SFR in galaxies in the AGN portion of the BPT diagram in the limiting cases of very low SFR.

[3] The post-burst age will be shorter than the time since the beginning of the burst and results in some cases of small negative ages in galaxies for which the best-fit SFH has a still-declining burst

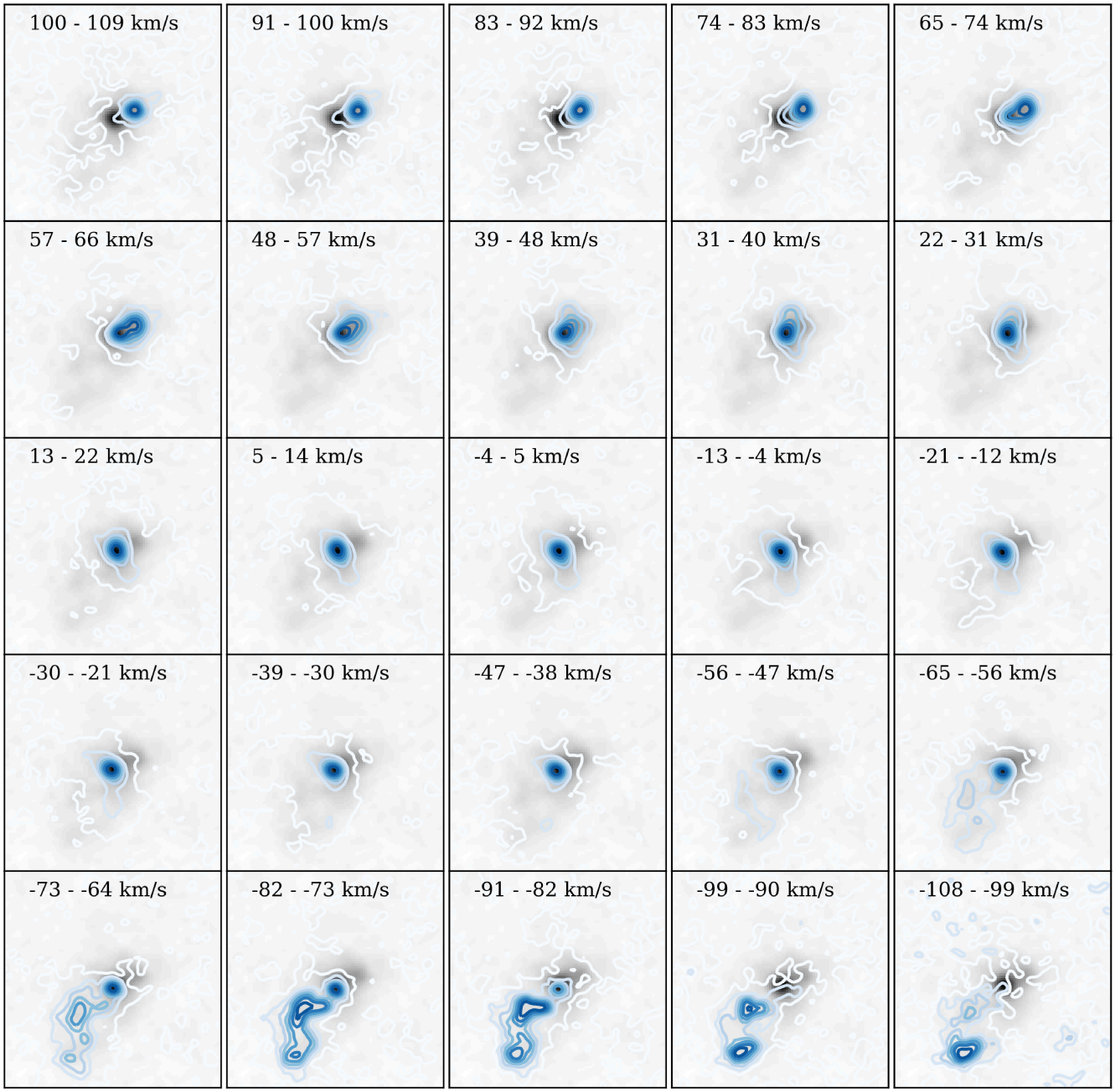

Figure 7. CO (3-2) channel maps for S02, grouped by velocity bin (blue contours). Each image is $4 \times 4''$. In greyscale, the full moment zero map is shown for reference. A blueshifted outflow is seen to the lower left of the galaxy at velocities $\sim$ -64 – -108 km s^{-1}, in the bottom row of this Figure. This component is roughly in line with the rotational axis of the gas in the rest of the galaxy (and the stellar velocity observed from MaNGA observations). The velocity range shown here is symmetric, and yet only a blueshifted outflow is seen without a redshifted counterpart.

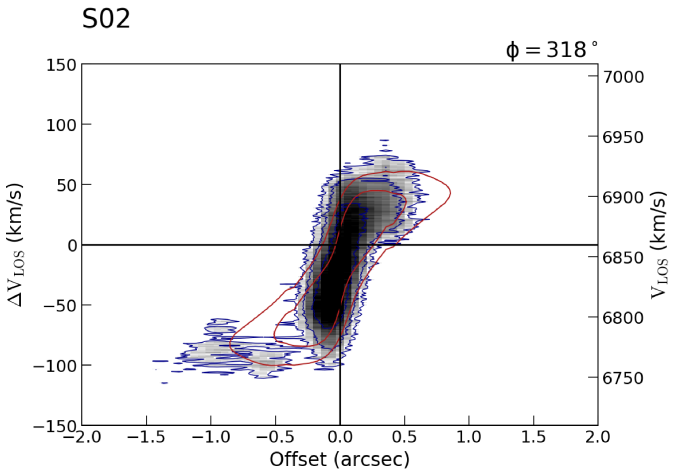

Figure 8. Position-Velocity diagram along major axis (from MaNGA stellar velocity field), with best-fit model from Barolo (Di Teodoro & Fraternali 2015) overplotted in red contours. The blueshifted feature observed above in the moment maps is distinct from the rest of the molecular gas in the galaxy, suggesting it is an outflow rather than a continuation of a rotating disk.

We explore the evolution during the post-starburst phase quantitatively by fitting the sSFR and CO-traced molecular gas fraction trends with two-component linear fits to $x - ln(y)$, with the two lines required to meet in the middle. For the sSFR - age comparison, the best fit early slope is 65 Myr, the best fit late slope is 480 Myr, and the pivot point is 77 Myr. The best fit early slope is comparable to the typical duration of the recent bursts (French et al. 2018a) and may be a continuation of the decline in SFR as the burst ended. Given the uncertainties on the derived parameters, the early and late slopes are significantly different. In contrast, fitting the same two-component function to the CO-traced gas fraction - age comparison, there is no significant difference between the early and late slope. We see no evidence to support a two-phase evolution in the decline of the CO-traced gas with time. These lines are overplotted on Figure 11.

The dense molecular gas to total molecular gas fraction, traced by the $L'_{\rm HCO+}/L'_{\rm CO}$ ratio, is proportional to the fraction of the molecular gas reservoir in the denser states probed by HCO^+. In several cases, the post-starburst galaxies show evidence that the $L'_{\rm HCN}$ luminosity is enhanced relative to the $L'_{\rm HCO+}$, similar to many AGN and ULIRGs (see further discussion in §3.6), so we consider $L'_{\rm HCO+}$ here as a more accurate tracer of the dense gas mass. Most (5/6) of the post-starburst galaxies have low ($L'_{\rm HCO+}/L'_{\rm CO} < 0.04$) fractions, except for R02, which is the youngest post-starburst galaxy in our ALMA-targeted sample. This may indicate a rapid ($<<$ 100 Myr) decline in the dense gas fraction at the start of the starburst, but a larger sample will be required to determine whether this trend is significant, as it is driven by the observations for a single galaxy. If we instead consider the dense gas to stellar mass fraction, using an $\alpha_{HCO^+} = 10\ M_\odot\ ({\rm K\,km\,s^{-1}\,pc^2})^{-1}$, this rapid decline is not observed. These differing trends may be caused by scatter in the CO-traced gas fraction amongst the sample. Observations of a larger sample will be required to determine whether the dense molecular gas has a rapid early decline similar to that seen in the sSFR, or a slower decline throughout the post-starburst phase more like the evolution seen in the CO-traced gas.

3.5. *Star Formation in the Dense Gas*

Previous work on the dense gas in post-starburst galaxies were motivated by the high CO luminosities relative to the low SFRs. In Figure 12, we plot $L'_{\rm CO}$ vs. SFR for post-starburst galaxies and comparison samples of other galaxy types. We consider the Hα-traced SFRs for the post-starburst sample here; the impact of SFR tracer on our results is explored further in S4.1 and in Appendix B. The post-starburst galaxies are systematically offset to higher $L'_{\rm CO}$ relative to other quiescent galaxies (French et al. 2015). The two highest SFR post-starbursts shown are R02 and R05, from the Rowlands et al. (2015) sample, which uses a different selection method (see §2.1). These are also the youngest post-starburst galaxies considered here and have $L'_{\rm CO}$ values consistent with the SFRs. The location of these young post-starbursts on the $L'_{\rm CO}$–SFR relation is consistent with the evolution of the star formation efficiency ($\propto SFR/L'_{\rm CO}$) seen by Li et al. (2019).

Our previous study of the dense gas in two post-starburst galaxies (H02, S05 French et al. 2018b) found low limits on $L'_{\rm HCN}$ and $L'_{\rm HCO+}$, consistent with their low SFRs. Here, we primarily consider the $L'_{\rm HCO+}$ instead of $L'_{\rm HCN}$ to trace the dense gas, as the HCN is likely overestimating the dense gas mass (see further discussion in §3.6), although both are shown in Figures 12 and 13. For the four new post-starburst galaxies targeted in this study, we find that the two young post-starburst galaxies from the Rowlands et al. (2015) parent sample (R02 and R05) also have dense gas luminosities consistent with their SFRs (Figure 12). For the two older post-starburst galaxies from the French et al. (2015) parent sample, S02 is not detected in either HCN+ or HCN, at levels either consistent with its low SFR or slightly above. H03 remains offset from the $L'_{\rm HCO+}$–SFR relation, but the SFR of this galaxy is highly uncertain (see discussion in §4.1).

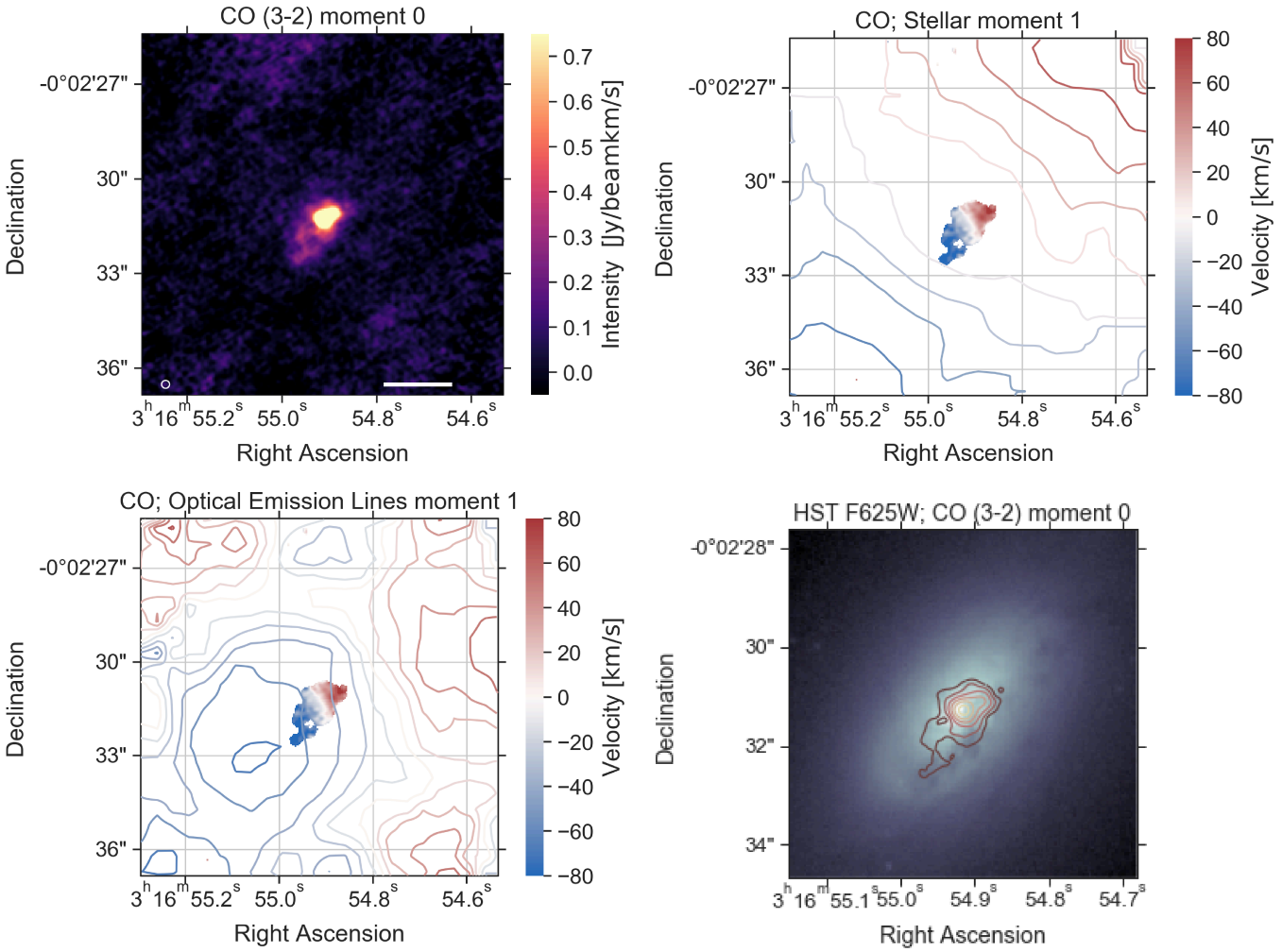

Figure 9. ALMA CO (3–2) observations of S02 with complementary MaNGA (Bundy et al. 2015) observations (MaNGA plateID 8080-3072) accessed via Marvin (Cherinka et al. 2019). Top left: CO (3–2) moment 0 map, with beam size shown in bottom left. The galaxy has a faint trail of gas extending to the lower left. Top right: CO (3–2) moment 1 map, with stellar velocity contours from MaNGA overlaid in the same color scale. The stellar velocity is aligned with the bulk of the molecular gas velocity. The faint component to the lower left is blueshifted with respect to the surrounding stellar velocity field, indicative of an outflowing component. Bottom left: CO (3–2) moment 1 map, with optical emission line velocity contours from MaNGA overlaid in the same color scale. The ionized gas is disturbed with respect to the stellar velocity. The blueshifted CO component is aligned with the blueshifted ionized gas region, indicating a multiphase outflow. Bottom right: Comparison of CO (3–2) moment 0 map with *HST* F625W image. The blueshifted component to the lower left is aligned with a dust lane in the *HST* image.

We consider the ratio of dense molecular gas to total molecular gas traced by $L'_{\rm HCO+}/L'_{\rm CO}$ in Figure 13. The post-starburst galaxies have low values of $L'_{\rm HCO+}/L'_{\rm CO}$, except for the youngest post-starburst galaxy in the sample, R02. As discussed in §3.4, this may be an evolutionary effect with post-burst age. In French et al. (2018b), we observed low HCN/CO ratios from two of the HCN limits plotted here. With the addition of the four new galaxies, as well as the addition of the comparison sample of star-forming galaxy components from Usero et al. (2015), we see that 5/6 of the post-starbursts have low HCN/CO ratios relative to the comparison samples, though there are some star-forming galaxy components with lower HCN/CO ratios. The post-starburst galaxy with high HCN/CO (H03) may have HCN luminosity increased via mechanical heating or cosmic ray heating, as it has a very high HCN/HCO+ ratio (see discussion in §3.6). Given the low HCO+ luminosity of this galaxy, it is likely that the dense gas fraction is low.

3.6. *Dense Gas State*

Ratios between the dense gas tracers HCN, HCO+, and HNC (1–0) are sensitive to various mechanisms

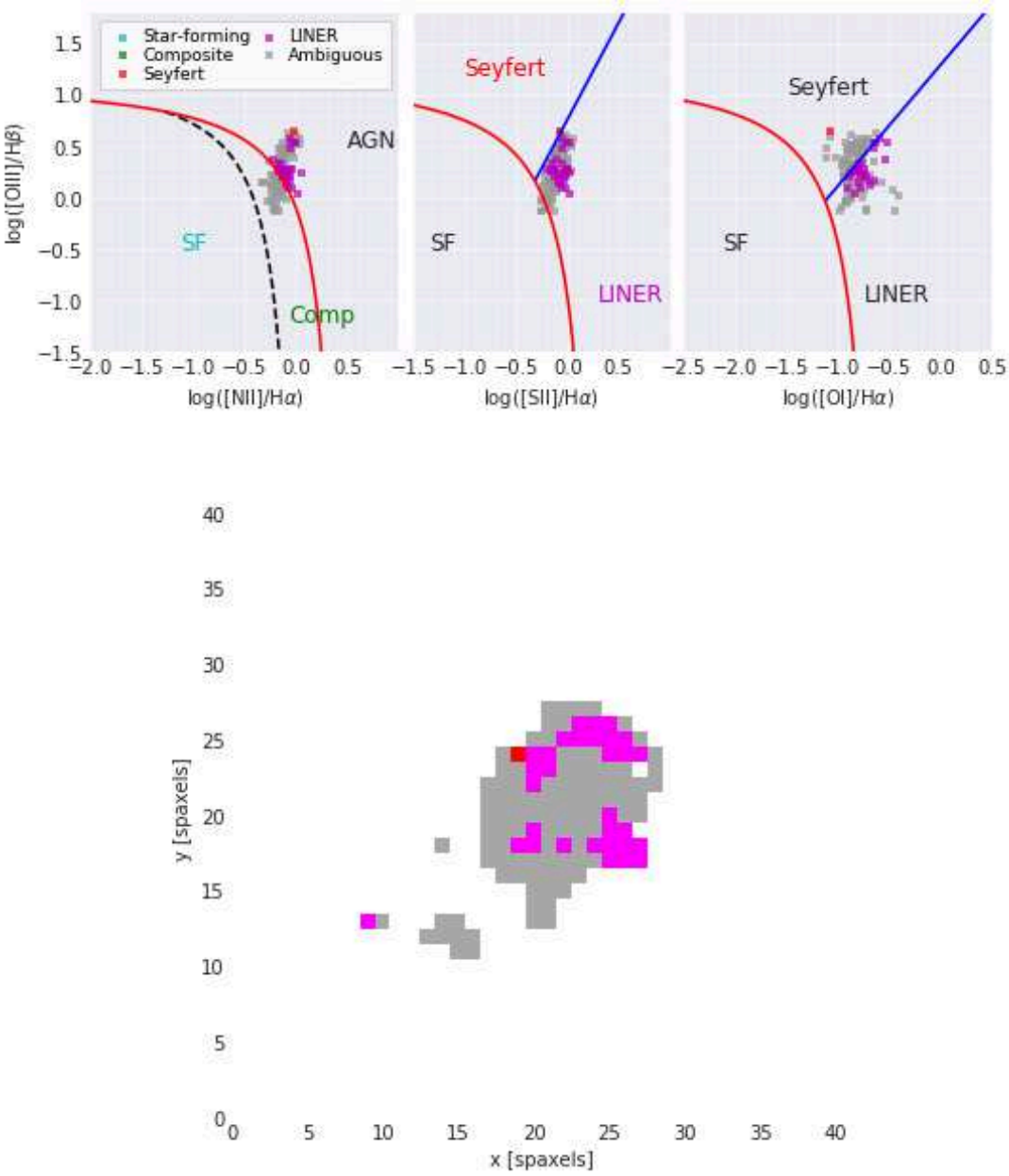

Figure 10. Resolved BPT (Baldwin et al. 1981) diagrams (top row) for S02, shown with diagnostic lines from Kewley et al. (2001) and Kauffmann et al. (2003). Each spaxel is classified using its emission line ratios. The bottom plot shows the spatial distribution of the spaxels colored by classification. Most of the galaxy has low emission line fluxes such that the classification is ambiguous, but the spaxels that can be classified are in the LINER part of the BPT diagram (with one Seyfert spaxel). This LINER-like signature extends outside of the nucleus over ~ 5 arcsec (10 spaxels), significantly more than the 2.5 arcsec FWHM of MaNGA's spatial resolution (Law et al. 2016). It is thus more likely to be caused by post-AGB stars (Yan & Blanton 2012) or shocks (Rich et al. 2015) than current AGN activity. This galaxy does not have current AGN activity. However, the flickering timescale for AGN is shorter than the characteristic timescale of the outflow, so the outflow could have been launched by a previous episode of AGN activity.

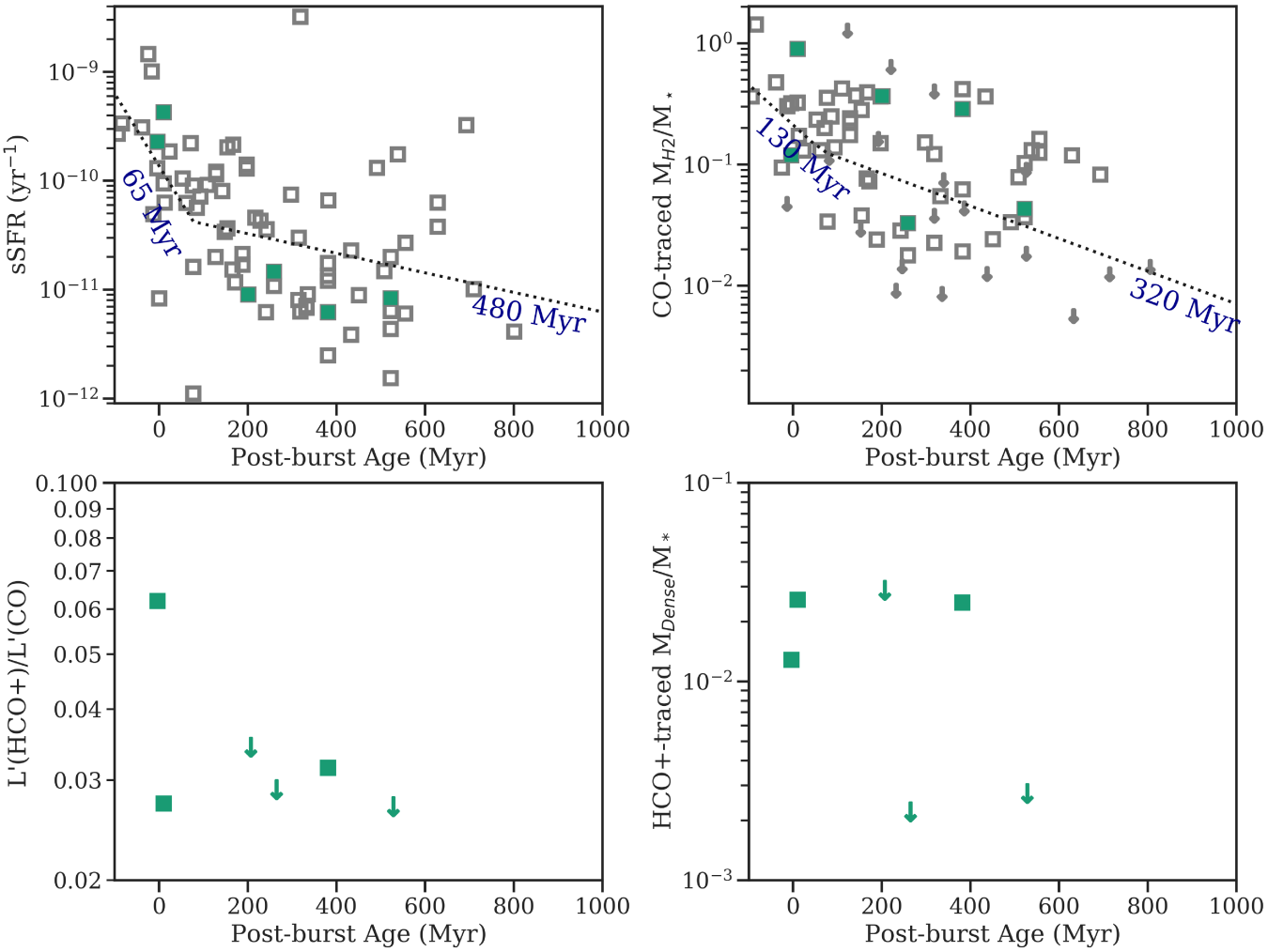

Figure 11. Trends of specific SFR, molecular gas fraction (traced by CO (1-0)), and dense gas fraction (traced by HCO^+/CO (1-0) vs. post-starburst age (French et al. 2018a). The ALMA targets considered in this study are highlighted in green. (Top left): SFR (traced by Hα) for galaxies with CO observations from French et al. (2015), Rowlands et al. (2015), and Alatalo et al. (2016). We fit these data using a two-component exponential decline (dotted line), finding a significant difference in the early vs. late time slopes (timescales indicated on figure). (Top right): CO-traced molecular gas to stellar mass fraction (assuming αCO = 4) for galaxies from French et al. (2015); Rowlands et al. (2015); Alatalo et al. (2016). Using the same two-component model, we observe no significant difference in the early vs. late timescales in the CO-traced gas fraction. The time evolution of the CO-traced gas fraction is consistent with a single component model, unlike the sSFR trend. (Bottom left): Dense gas fraction traced by HCO^+/CO for the six PSBs considered here. Dense gas ratio (HCO^+/CO) suppression occurs throughout PSB phase and begins early (∼10-200 Myr after burst ends). Observations of a larger sample will be required to determine whether the dense molecular gas has a rapid early decline similar to that seen in the sSFR, or a slower decline throughout the post-starburst phase more like the evolution seen in the CO-traced gas. (Bottom right): The dense gas mass fraction normalized by stellar mass does not appear to decline as steeply as the HCO+/CO ratio, as the dense gas mass fraction of H03 remains high.

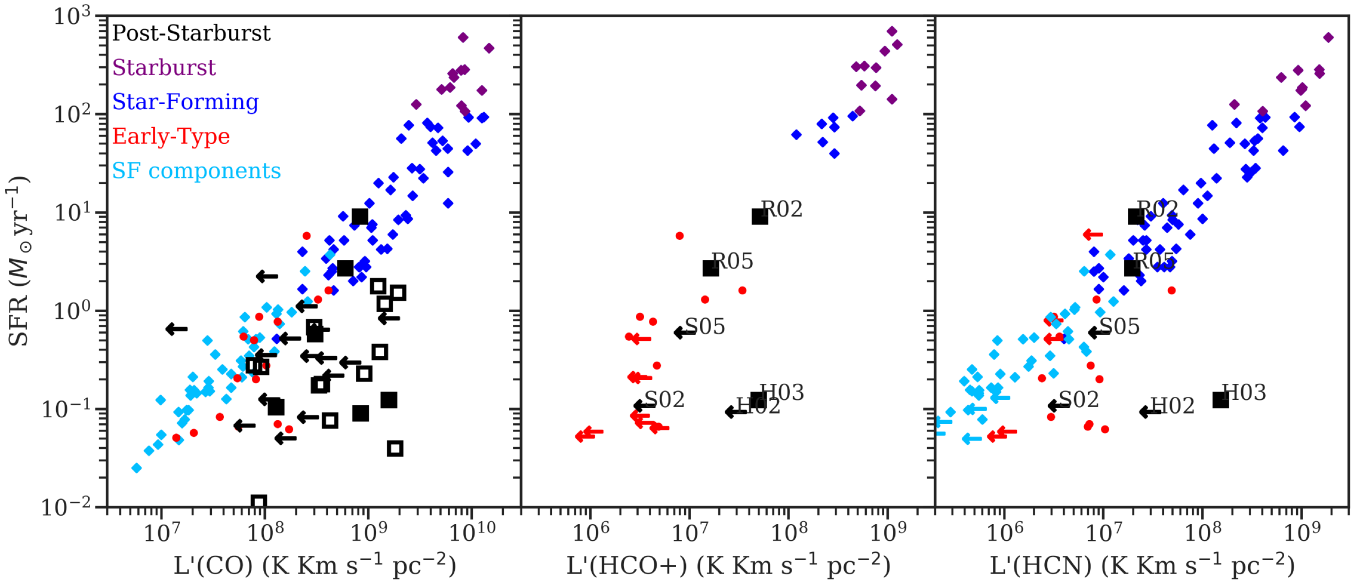

Figure 12. (Left:) $L'_{\rm CO}$ vs. SFR. Early type galaxies (Crocker et al. 2012), starburst and star-forming galaxies (Gao & Solomon 2004), and star forming galaxy components (Usero et al. 2015) are correlated with low scatter, but post-starburst galaxies (French et al. 2015) have low SFRs for their CO luminosities. Black squares indicate post-starburst detections and arrows indicate 3σ upper limits. Filled squares indicate the ALMA targets considered here (including two galaxies from the Rowlands et al. (2015) sample). SFRs for the post-starburst galaxies are measured using Hα emission (see §2.3). (Middle:) $L'_{\rm CO}$ vs. SFR for the same samples of galaxies. (Right:)$L'_{\rm HCN}$ vs. SFR for the same samples of galaxies. The post-starburst galaxies are more consistent with the comparison samples in their dense gas - star formation relations, with the exception of H03, which has a highly uncertain SFR (see full discussion in §4.1. The post-starburst galaxies have dense molecular gas properties consistent with either early type galaxies or lying between the star-forming and early type samples.

that affect the reliability of these lines as tracers of the dense gas mass. AGN and some ULIRGs have high HCN/HCO+ ratios (Kohno et al. 2001; Imanishi et al. 2004, 2007; Privon et al. 2015), which have been attributed to (1) IR pumping, (2) XDR (X-ray dominated region)-dominated chemistry, (3) mechanical heating, or (4) cosmic ray heating (Aalto et al. 2007; Loenen et al. 2008; Meijerink et al. 2011; Bayet et al. 2011; Privon et al. 2015, 2020).

We compare the HCN/HCO+ ratios of the three post-starburst galaxies with both line measurements with other types of galaxies in Figure 14. The HCN/HCO+ ratios of the post-starburst galaxies vary considerably, with scatter across the entire sample of comparison galaxies. This scatter is much larger than the uncertainty on the line ratio measurements. One of the PSBs (H03) has a very high HCN/HCO+ ratio (low HCO$^+$/HCN), even compared to AGN and ULIRGs.

We consider each of the possibilities for increasing the HCN/HCO+ ratio listed above, and thus driving the large scatter in HCN/HCO$^+$ across the post-starburst sample. IR pumping is not a likely cause, as the IR flux is much lower in these galaxies. H03 has a total IR luminosity of $< 10^{11}$ L$_\odot$, less than the criterion for a LIRG. The HNC/HCN ratio is sensitive to the ionization state of the ISM, and can distinguish XDRs from PDRs (photon dominated regions). We plot the comparison of the HCN, HCO+, and HNC (1–0) ratios in Figure 15. The PSBs have similar HNC/HCN values as most of the starbursts, and are consistent with PDR-dominated ionization.

Mechanical heating or cosmic ray heating from past AGN activity are the most likely causes for the high HCN/HCO+ ratio in H03. While the source of the mechanical heating in starburst galaxies has been suggested to be YSOs/SN winds (Loenen et al. 2008), the low SFRs in the post-starburst galaxies may indicate a different source, such as shocks. Furthermore, no correlation is observed between the HCN/HCO+ ratio and the star formation rate in our sample or in other galaxies (Privon et al. 2015), suggesting star formation does not drive the high HCN/HCO+ ratio. This may be related to the turbulent heating found by Smercina et al. (2021) for other post-starburst galaxies.

No clear correlation has been observed between the HCN/HCO+ ratio and the strength of the AGN activity, traced by Privon et al. (2015) using the PAH 6.2μm feature. However, the timescale of flickering AGN activity is faster than the timescale for the dense gas tracers to be affected (Privon et al. 2020). While there is only weak

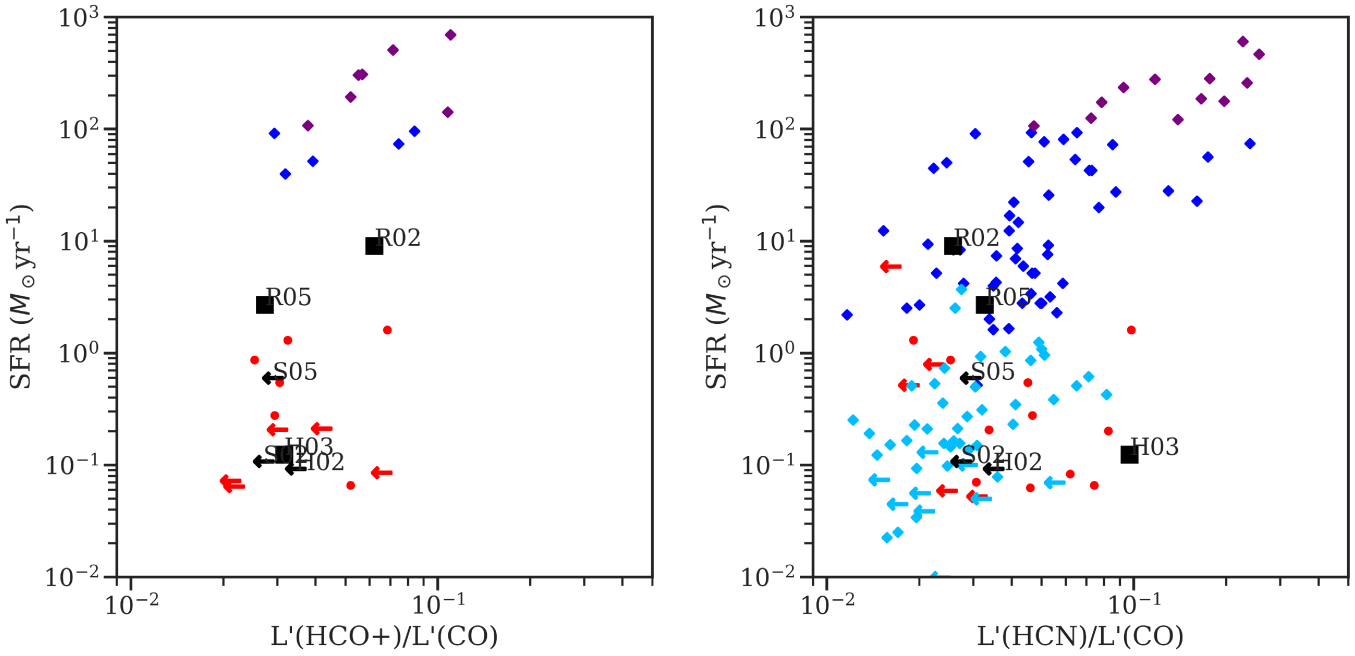

Figure 13. (Left:) Dense gas luminosity ratio $L'_{\rm HCO+}/L'_{\rm CO}$ for the same samples as Figure 12. Post-starburst galaxies have low ratios of dense molecular gas to total molecular gas compared to other types of galaxies, although this may evolve rapidly with time during the early post-starburst phase (Figure 11). (Right:) Dense gas luminosity ratio $L'_{\rm HCN}/L'_{\rm CO}$ for the same samples. The post-starburst galaxy with high HCN/CO (H03) may have HCN luminosity increased via mechanical heating or cosmic ray heating, as it has a very high HCN/HCO+ ratio (see discussion in §3.6), and the HCN/CO ratio may overestimate the dense molecular gas fraction.

evidence for current AGN activity in the post-starburst galaxies, past AGN activity may be affecting the dense gas state for the post-starburst galaxies considered here as well as starburst galaxies.

4. DISCUSSION

4.1. *Star Formation Rates*

The measurement of current SFRs in post-starburst galaxies is complicated by a number of factors (see discussion in French 2021 §5). For this work, our goal is to measure the current SFR (over timescales < 10 Myr), with low contamination from other sources of excitation, and with accurate correction applied for dust extinction. Contamination from the young stellar populations, AGN, and shocks would cause SFRs to be over-estimated, while high dust obscuration beyond that probed by Balmer decrement corrections would cause the SFRs to be under-estimated. We consider here the comparison of the Hα-based SFRs used above (described in §2.3) to other SFR tracers to assess the possible biases in these measurements.

The combination of the [NeII] 12.8μm and [NeIII] 15.6μm lines traces HII regions with relatively low bias compared to other SFR tracers (Ho & Keto 2007; Whitcomb et al. 2020). Dust extinction scales as $A_\lambda/A_V \sim \lambda^{-2}$ in the near- and mid-IR; using the extinction law measured by (Wang & Chen 2019), the extinction at the wavelengths of [NeII] and [NeIII] is $500 - 800\times$ lower than A_V. Thus, the Neon-based SFRs will not be subject to underestimation due to dust obscuration, even in galaxies with ULIRG-like central dust obscuration. Smercina et al. (2018) measured Neon-based SFRs for a sample of 15 post-starburst galaxies, two of which (S02 and S05) are studied in this work. We compare the Neon-based SFRs to Hα-based SFRs in Figure 16. No systematic bias is observed; of the two galaxies considered here, the measurements of S02 agree well, and the Neon-based SFR for S05 is lower than the Hα SFR. This indicates that neither galaxy has significant obscured star formation. In section B, we consider the impact of using Neon-based SFRs on the Kennicutt-Schmidt relation, finding the post-starburst galaxies to lie offset from the relation formed by star forming and starburst galaxies, consistent with the results from using Hα-based SFR tracers.

The TIR luminosity is also sensitive to obscured star formation, yet the TIR traces star formation on longer timescales, which can be comparable to the time since the recent starburst. Smercina et al. (2018) found that TIR-based SFRs overestimate the SFR from Neon by a factor of ~ 2; a similar factor of two offset is observed by Kennicutt (1998) in the comparison between

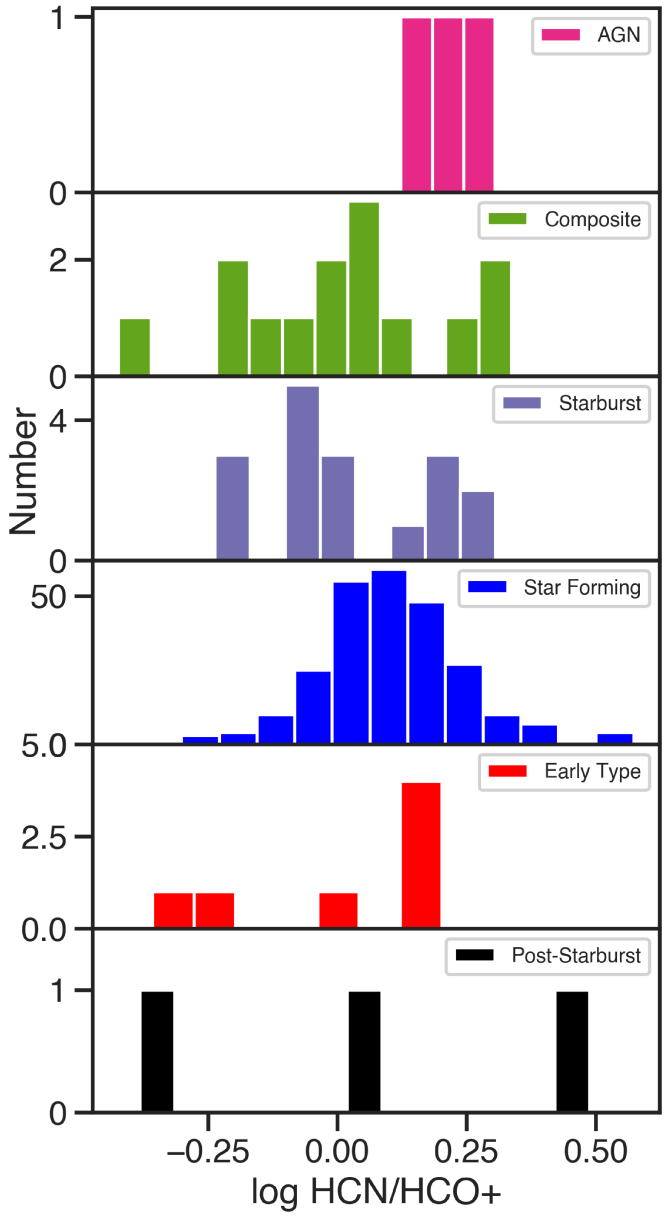

Figure 14. Histograms of HCN/HCO$^+$ ratios for different galaxy types. LIRGs from Privon et al. (2015) are divided in to AGN, composite, and starbursting based on their PAH 6.2μ EWs (Stierwalt et al. 2013). Components of massive star-forming galaxies are from Jiménez-Donaire et al. (2019). Early type galaxies are from Crocker et al. (2012). Only galaxies with significant detections in both lines are plotted here. Privon et al. (2015) found that while the HCN/HCO$^+$ ratio is enhanced in AGN, likely due to mechanical heating, other galaxies may have high HCN/HCO$^+$ ratios without signs of current AGN activity. This may be due to the short duration of AGN signatures compared to the effect on the dense gas, or other processes affecting the dense gas state. One post-starburst galaxy (H03) has a HCN/HCO$^+$ ratio as high as the AGN from Privon et al. (2015), which may indicate buried or past AGN activity. One post-starburst (R02) has a lower HCN/HCO$^+$ ratio than almost all other comparison galaxies with both lines detected. The HCN/HCO+ ratios of the post-starburst galaxies vary considerably, with scatter across the entire sample of comparison galaxies. This scatter is much larger than the uncertainty on the line ratio measurements.

TIR-based SFRs and Br-γ SFRs in starburst galaxies. This is likely caused by the longer duration of star formation traced by the TIR luminosity, from the heating of dust by the young A star population. We compare the Hα-based SFRs to TIR-based SFRs from Smercina et al. (2018) for the galaxies from French et al. (2015, H02, H03, S02, S05) and full SED fit SFRs (including *Herschel* photometry) from Rowlands et al. (2015) for R02 and R05 in Figure 16. The TIR-based SFRs are divided by a factor of two to account for heating from the young A star population, using the comparison of these SFRs provided by Smercina et al. (2018). With this correction, there is no systematic bias between the two SFR indicators, although the scatter is large. We note that for H02 and H03, the large offset indicates there may be obscured star formation. Recently, Baron et al. (2022) found that some samples of post-starburst galaxies have high SFRs $\sim 10-100$ M$_\odot$ yr^{-1} when traced by their IR luminosity. The samples most heavily affected are post-starburst samples chosen to optimize for young post-starburst ages or to not select against AGN activity. We note that the SFRs for the post-starburst galaxies considered here have significantly lower SFRs, even using the highest estimates from the TIR luminosity.

We compare the Hα-based SFRs to 1.4 GHz based SFRs using data from the VLA FIRST survey (Becker et al. 1995). We convert the 1.4 GHz fluxes and flux limits to SFRs following Nielsen et al. (2012) by using the calibrations from Condon (1992); Yun et al. (2001). Of the galaxies considered here, R02, R05, and H03 are detected by FIRST, and the rest of the galaxies are not detected. The 1.4 GHz flux is likely to be contaminated by any AGN or LINER activity in the post-starbust sample (e.g., Morić et al. 2010), especially for H03, given the large offset between the 1.4 GHz and Brγ indicators.

Another infrared line used to calculate SFRs with minimal effects from dust attenuation is the Brγ line (see Pasha et al. 2020). We have conducted a survey of NIR spectroscopy of the parent samples considered here from French et al. (2015); Rowlands et al. (2015); Smercina et al. (2018) using Magellan/FIRE (Tripathi, French et al. in preparation). Using the calibration from Kennicutt (1998), we compare the Brγ SFRs to the Hα SFRs in Figure 16. Brγ is detected for R02 and R05. Our data provide useful upper limits on the SFRs for H03 and S02[4]. Despite the high SFR ~ 5 M$_\odot$ yr^{-1} for H03 that would be inferred from its TIR or 1.4 GHz luminosities, H03 is not detected in Brγ, at a level consistent

[4] Unfortunately, the faint K-band magnitude of H02 prohibited its inclusion in the FIRE sample.

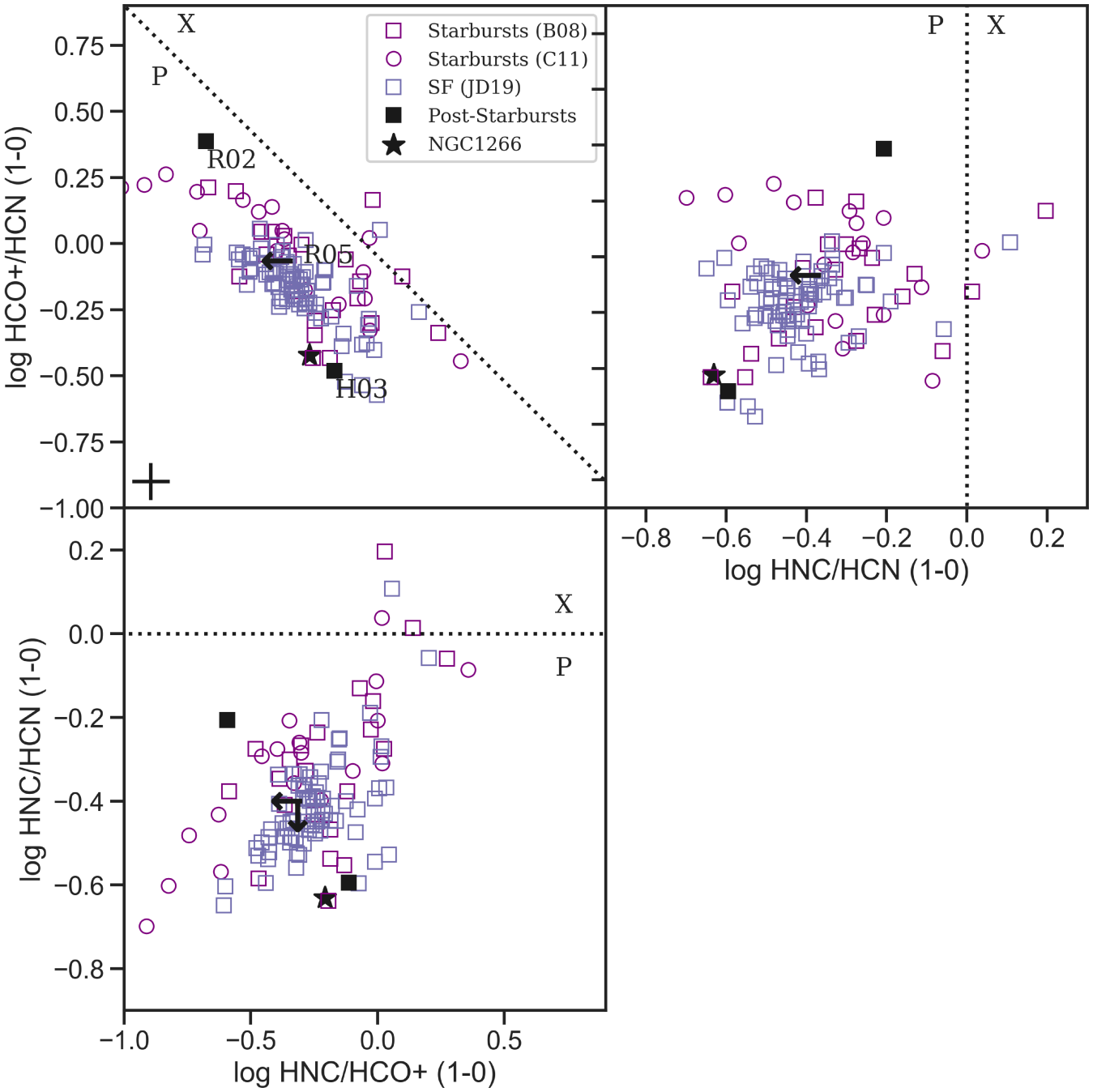

Figure 15. Ratios of dense gas tracers HCN (1-0), HCO^+ (1-0), and HNC (1-0) (adapted from Baan et al. 2008; Loenen et al. 2008). Post-starburst galaxies from this study are shown with comparison starburst samples (Baan et al. 2008; Costagliola et al. 2011), comparison components of massive star-forming galaxies (Jiménez-Donaire et al. 2019), and the shocked post-starburst galaxy NGC 1266 (K. Alatalo, private communication). A characteristic errorbar is shown in the top left panel. The HNC/HCN ratio is sensitive to the ionization state of the ISM, and can distinguish XDR from PDR dominated regions (dotted lines). The PSBs, like most of the starbursts, are consistent with PDR-dominated ionization. HCN/HCO^+ ratio varies as much within the PSB sample as within ULIRGs. The low HCO^+/HCN ratios of the PSBs are consistent with mechanical heating as modelled by Loenen et al. (2008).

with its Hα flux. This unusual TIR/Brγ ratio is not seen for other galaxies, even those with extremely high extinction like Arp 220 (Pasha et al. 2020). Further observations, especially Near- and Mid- IR spectroscopy, will be required of these sources to determine the origin of the dust heating. While in French et al. (2018b) we assigned an upper limit on the SFR for H02, here we use the Hα-based SFRs throughout, motivated by the consistency with the Brγ observations.

The Neon-based SFRs are the best available SFR tracer for this sample, as the Neon lines can trace obscured star formation even at the levels of ULIRGs, the contamination from other excitation sources is low, and the timescale for this SFR tracer is much shorter than the typical post-starburst ages (Ho & Keto 2007; Smercina et al. 2018). Unfortunately, mid-IR spectroscopy is required for this measurement, and not available for the entire sample considered here. We use the cases where both Neon and Hα SFRs are available to test the Hα SFRs for bias (Figure 16) and find the two tracers to be consistent. This consistency indicates that the post-starburst galaxy samples considered here do not typically have obscured star formation missed by the Hα tracer corrected using the Balmer decrement. Two galaxies (H02 and H03) have strong mismatches between the TIR SFR and Hα SFR, yet do not have mid-IR spectroscopy for which a Neon SFR can be measured. For one of these galaxies (H03), we have a strong limit on the Brγ SFR, which is consistent with Hα. While Brγ is less sensitive to dust obscuration than Hα, ULIRG-like central dust densities could still obscure a nuclear star-forming region. Such a mismatch between a quiescent host galaxy and a nuclear starburst would be unusual, as LIRGs and ULIRGs have star-forming regions visible outside of the central regions with high dust obscuration, but we cannot fully rule out the possibility of an obscured region with SFR$\sim$ 5 $M_\odot$ yr^{-1} in H02 and H03.

In order to assess the impact of SFR tracer on our conclusions, we reproduce the key figures in this work using the TIR-based SFRs in Appendix §B. The SFRs for four galaxies (S02, S05, R02, R05) are comparable, while the SFRs for two galaxies (H02 and H03) are higher. Considering the TIR SFRs instead of the Hα SFRs, our qualitative conclusions do not change. We find that the post-starburst galaxies still lie offset from the Kennicutt-Schmidt relation, and have high $L'_{\rm CO}$ yet consistent $L'_{\rm HCO+}$ and $L'_{\rm HCN}$ values for their SFRs.

4.2. *Interpretation*

As galaxies evolve through the post-starburst phase, the galaxies with remaining molecular gas remaining experience an unusual transition in their gas properties. The gas is confined to the central ~kpc, more limited in extent than the optical light or even the young stellar populations. Yet the gas state is such that the typical density is low, as traced by both the lack of strong dense gas emission and by the low CO excitation. What then is suppressing this gas from collapsing to denser states?

The low CO excitation indicates that the bulk of the molecular gas is not being heated. The outflow observed in S02, as well as the outflow observed in CO (2–1) by Smercina et al. (2021) for another post-starburst, provide a clue that relatively low velocity outflows, lower than or close to the escape velocity, may prevent the gas from re-collapsing. The origin of these outflows is still unclear. We observe no strong AGN activity in these galaxies, yet because the timescale for AGN to vary is shorter than the timescale for us to observe these outflows, past AGN activity may have launched these outflows. Alternatively, weak, low-level AGN activity (if the LINER is a low luminosity AGN) may be enough to sustain quiescence during this phase and deplete the gas over 1–2 Gyr. If weak AGN activity is currently affecting these galaxies, it must be at such a low level as to not result in high CO excitation and not drive AGN-like emission line ratio maps. We speculate that if the energy coupling of TDEs to the molecular gas is efficient compared to AGN energy coupling, the high TDE rate during this phase may act to provide the energy source needed to keep this gas from collapsing to denser states and forming stars (see further discussion in Smercina et al. 2021).

A key test for models of feedback in simulations aiming to re-create the galaxy population, including galaxies with rapidly-ending star formation, will be to predict the detailed evolution of the densest gas on scales of $n \sim 10^4$ cm^{-3} and at cold temperatures $T < 100$ K.

5. CONCLUSIONS

Observations of large fractions of molecular gas remaining in galaxies with recently-ended starbursts have raised questions of what mechanisms act to drive galaxies to quiescence. In this study, we present new observations of CO (3–2) observations for three post-starburst galaxies and dense gas tracers for four post-starburst galaxies, combining with literature measurements for a total dense gas sample size of six.

1. The post-starbursts have low excitation as traced by the CO spectral line energy distribution (SLED) up to CO (3–2), more similar to early-type than starburst galaxies. The low excitation indicates that lower density rather than high temperatures may suppress star formation during the post-starburst phase, as higher temperatures

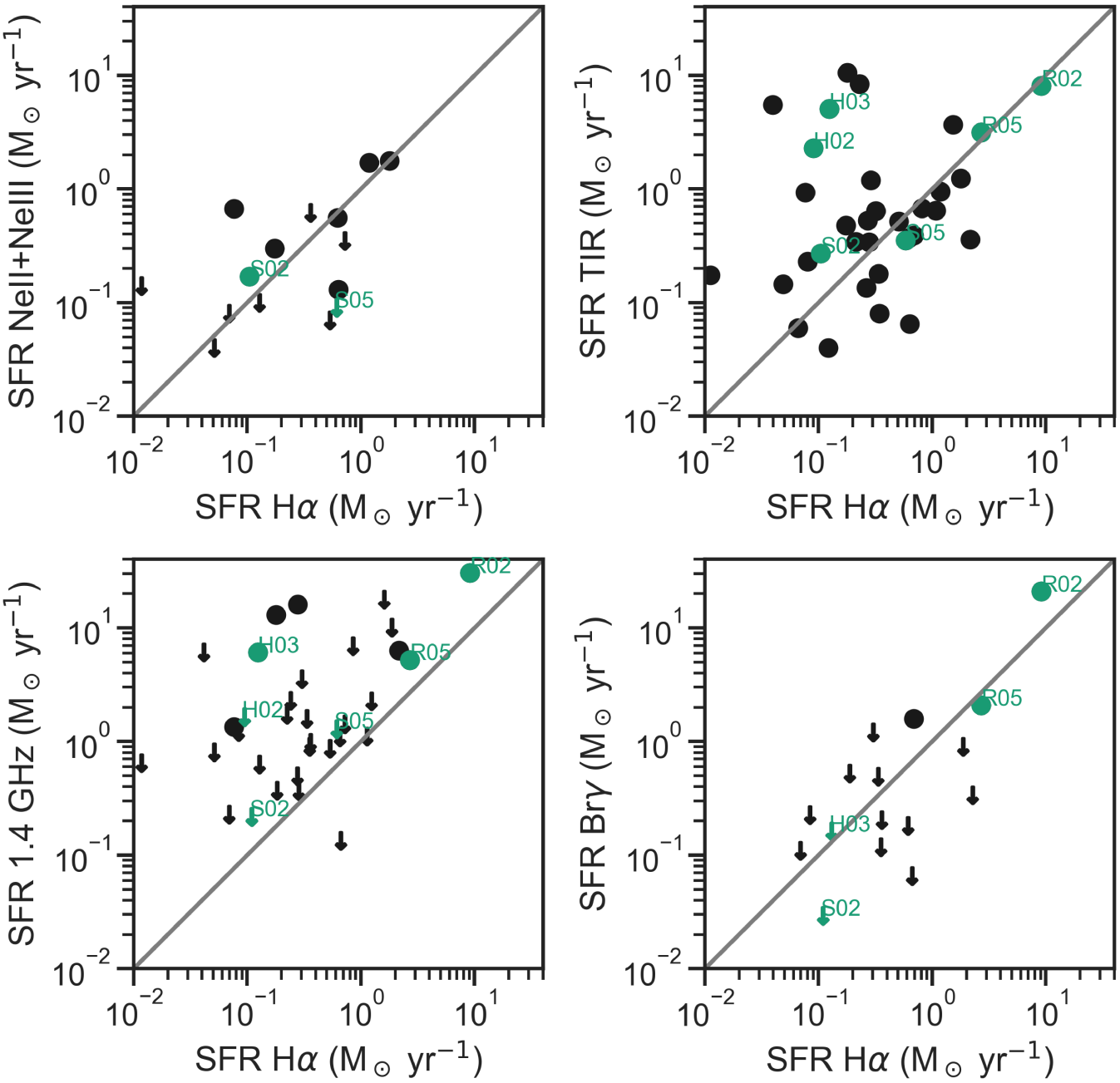

Figure 16. Comparison of SFR tracers (discussed in §4.1) with the Hα-based SFRs used elsewhere in this study. Post-starburst galaxies from French et al. (2015); Rowlands et al. (2015); Smercina et al. (2018) are shown in black, and the ALMA targets are highlighted in green. All limits are 3σ upper limits. The Hα SFRs are consistent with short-duration infrared tracers from Neon and Brγ, indicating that the use of Hα is not biased low due to dust obscuration. Smercina et al. (2018) observed a systematic offset between TIR and Neon SFRs, such that the TIR-based SFRs were on average 2× higher than the Neon SFRs, likely due to dust heating by young stars. We apply this correction to the TIR SFRs used here.

would result in excitation states more like starbursts. Radiative transfer modelling with RADEX supports this picture; the RADEX models favor low densities ($\log n/\mathrm{cm}^{-3} \sim 3.4 - 3.8$) and temperatures ($T \sim 15 - 30$ K), similar to early type galaxies and lower than typical starbursts. The low CO excitation is in contrast with the high ISRF intensity (and thus high dust temperatures) in these galaxies, suggesting the molecular gas temperature is decoupled from the dust.

2. The post-starburst galaxies have small CO (3–2) sizes ($\sim 250 - 400$ pc) compared to their optical sizes. The CO (3–2) sizes are on average 6.3× smaller than the r-band optical sizes from SDSS images. This result is consistent with the findings of Smercina et al. (2021).

3. Post-starburst galaxies have high molecular gas surface densities for their star formation rate surface densities, resulting in an offset from the Kennicutt-Schmidt relation, consistent with the findings of Smercina et al. (2021). We find this same result using both optical (Hα) and infrared SFR tracers (TIR luminosity and [NeII] 12.8μm + [NeIII] 15.6μm), indicating that this offset is not driven by the presence of dust-obscured star formation.

4. One galaxy (S02) displays a blueshifted molecular gas outflow traced by CO (3–2). This galaxy has complementary *HST* and MaNGA observations, facilitating multiwavelength comparisons. The MaNGA observations show the ionized gas velocity is disturbed relative to the stellar velocity field, with a blueshifted component aligned with the molecular gas outflow, indicative of a possible multiphase outflow. The inferred mass loss rate is consistent with the CO depletion observed statistically in French et al. (2018a). The energy required to drive this outflow is consistent with lower luminosity AGN/LINERs or TDEs. The feasibility of energy from intermittent AGN activity or from TDEs will depend heavily on the coupling to the molecular gas in these galaxies.

5. Low ratios of $\mathrm{HCO}^+/\mathrm{CO}$, indicating low fractions of dense molecular gas relative to the total molecular gas, are seen throughout the post-starburst phase beginning ∼10-200 Myr after burst ends. Most post-starbursts have low $\mathrm{HCO}^+/\mathrm{CO}$ ratios; the exception is the youngest post-starburst in our sample, suggesting early evolution. Rapid evolution in the dense gas would be consistent with the rapid evolution in sSFR during the early post-starburst phase. However, observations of a larger sample will be required to determine whether the dense molecular gas has a rapid early decline similar to that seen in the sSFR, or a slower decline throughout the post-starburst phase, more like the evolution seen in the CO-traced gas.

6. Post-starburst galaxies have low $L'_{\mathrm{HCO+}}$-traced dense gas luminosities more consistent with their low SFRs than the CO luminosities would indicate, with the exception of the post-starburst galaxy H03 which has a highly uncertain SFR. This is consistent with our previous work (French et al. 2018b) and indicates that the low SFRs in the post-starburst phase are due to a lack of dense gas, in contrast to the large masses of total molecular gas traced by CO (1–0) (French et al. 2015; Rowlands et al. 2015; Alatalo et al. 2016). Our qualitative conclusions do not depend on the SFR tracer used.

7. The three post-starbursts with measured $\mathrm{HCN}/\mathrm{HCO}^+$ ratios show a large variation, spanning the entire range shown by AGN, ULIRGs, and star forming galaxies. This may be due to a range of either mechanical heating or cosmic ray heating of the HCN, but the origin is uncertain.

We thank Antonio Usero and Adam Leroy for providing star forming galaxy comparison observations. K.D.F. thanks Dalya Baron for valuable discussions on the SFR tracers. A.S. was supported by NASA through grant #GO-14610 from the Space Telescope Science Institute, which is operated by AURA, Inc., under NASA contract NAS 5-26555. D.N. acknowledges support from NSF grant AST-1908137. Y.Y.'s research was supported by the Basic Science Research Program through the National Research Foundation of Korea (NRF) funded by the Ministry of Science, ICT & Future Planning (NRF-2019R1A2C4069803).

This paper makes use of the following ALMA data: 2016.1.00881, 2017.1.00930, 2017.1.00925, 2018.1.00948. ALMA is a partnership of ESO (representing its member states), NSF (USA) and NINS (Japan), together with NRC (Canada), MOST and ASIAA (Taiwan), and KASI (Republic of Korea), in cooperation with the Republic of Chile. The Joint ALMA Observatory is operated by ESO, AUI/NRAO and NAOJ. The National Radio Astronomy Observatory is a facility of the National Science Foundation operated under cooperative agreement by Associated Universities, Inc.

Funding for the Sloan Digital Sky Survey IV has been provided by the Alfred P. Sloan Foundation, the U.S. Department of Energy Office of Science, and the Participating Institutions.

SDSS-IV acknowledges support and resources from the Center for High Performance Computing at the University of Utah. The SDSS website is www.sdss.org.

SDSS-IV is managed by the Astrophysical Research Consortium for the Participating Institutions of the SDSS Collaboration including the Brazilian Participation Group, the Carnegie Institution for Science, Carnegie Mellon University, Center for Astrophysics — Harvard & Smithsonian, the Chilean Participation Group, the French Participation Group, Instituto de Astrofísica de Canarias, The Johns Hopkins University, Kavli Institute for the Physics and Mathematics of the Universe (IPMU) / University of Tokyo, the Korean Participation Group, Lawrence Berkeley National Laboratory, Leibniz Institut für Astrophysik Potsdam (AIP), Max-Planck-Institut für Astronomie (MPIA Heidelberg), Max-Planck-Institut für Astrophysik (MPA Garching), Max-Planck-Institut für Extraterrestrische Physik (MPE), National Astronomical Observatories of China, New Mexico State University, New York University, University of Notre Dame, Observatário Nacional / MCTI, The Ohio State University, Pennsylvania State University, Shanghai Astronomical Observatory, United Kingdom Participation Group, Universidad Nacional Autónoma de México, University of Arizona, University of Colorado Boulder, University of Oxford, University of Portsmouth, University of Utah, University of Virginia, University of Washington, University of Wisconsin, Vanderbilt University, and Yale University.

This research is based on observations made with the NASA/ESA Hubble Space Telescope obtained from the Space Telescope Science Institute, which is operated by the Association of Universities for Research in Astronomy, Inc., under NASA contract NAS 5–26555. These observations are associated with program 11643.

Software: Astropy (Astropy Collaboration et al. 2013, 2018), CASA (McMullin et al. 2007), Matplotlib (Hunter 2007), NumPy (Harris et al. 2020)

REFERENCES

Aalto, S., Garcia-Burillo, S., Muller, S., et al. 2012, Astronomy and Astrophysics, 537, 44

Aalto, S., Spaans, M., Wiedner, M. C., & Hüttemeister, S. 2007, A&A, 464, 193

Alatalo, K., Lisenfeld, U., Lanz, L., et al. 2016, The Astrophysical Journal, 827, 106

Astropy Collaboration, Robitaille, T. P., Tollerud, E. J., et al. 2013, A&A, 558, A33

Astropy Collaboration, Price-Whelan, A. M., Sipőcz, B. M., et al. 2018, AJ, 156, 123

Baan, W. A., Henkel, C., Loenen, A. F., Baudry, A., & Wiklind, T. 2008, Astronomy & Astrophysics, 477, 747

Baldwin, J. A., Phillips, M. M., & Terlevich, R. 1981, PASP, 93, 5

Baron, D., & Netzer, H. 2019, MNRAS, 486, 4290

Baron, D., Netzer, H., Lutz, D., Prochaska, J. X., & Davies, R. I. 2022, MNRAS, 509, 4457

Bayet, E., Williams, D. A., Hartquist, T. W., & Viti, S. 2011, MNRAS, 414, 1583

Bayet, E., Bureau, M., Davis, T. A., et al. 2013, MNRAS, 432, 1742

Becker, R. H., White, R. L., & Helfand, D. J. 1995, ApJ, 450, 559

Belli, S., Newman, A. B., & Ellis, R. S. 2019, The Astrophysical Journal, 874, 17

Bezanson, R., Spilker, J. S., Suess, K. A., et al. 2021, arXiv e-prints, arXiv:2111.14877

Bournaud, F., Daddi, E., Weiß, A., et al. 2015, A&A, 575, A56

Brinchmann, J., Charlot, S., White, S. D. M., et al. 2004, MNRAS, 351, 1151

Bundy, K., Bershady, M. A., Law, D. R., et al. 2015, ApJ, 798, 7

Carilli, C. L., & Walter, F. 2013, ARA&A, 51, 105

Cherinka, B., Andrews, B. H., Sánchez-Gallego, J., et al. 2019, AJ, 158, 74

Cicone, C., Maiolino, R., Sturm, E., et al. 2014, A&A, 562, A21

Condon, J. J. 1992, ARA&A, 30, 575

Costagliola, F., Aalto, S., Rodriguez, M. I., et al. 2011, A&A, 528, A30

Couch, W. J., & Sharples, R. M. 1987, Monthly Notices of the Royal Astronomical Society, 229, 423

Crocker, A., Krips, M., Bureau, M., et al. 2012, Monthly Notices of the Royal Astronomical Society, 421, 1298

Croton, D. J., Springel, V., White, S. D. M., et al. 2006, MNRAS, 365, 11

de los Reyes, M. A. C., & Kennicutt, Robert C., J. 2019, ApJ, 872, 16

D'Eugenio, F., van der Wel, A., Wu, P.-F., et al. 2020, MNRAS, 000, 1

Di Matteo, T., Springel, V., & Hernquist, L. 2005, Nature, 433, 604

Di Teodoro, E. M., & Fraternali, F. 2015, MNRAS, 451, 3021

Draine, B. T., & Li, A. 2007, ApJ, 657, 810

Draine, B. T., Dale, D. A., Bendo, G., et al. 2007, ApJ, 663, 866

Dressler, A., & Gunn, J. E. 1983, The Astrophysical Journal, 270, 7

French, K. D. 2021, PASP, 133, 072001

French, K. D., Arcavi, I., & Zabludoff, A. 2016, ApJL, 818, L21

French, K. D., Wevers, T., Law-Smith, J., Graur, O., & Zabludoff, A. I. 2020, SSRv, 216, 32

French, K. D., Yang, Y., Zabludoff, A., et al. 2015, The Astrophysical Journal, 801, 1

French, K. D., Yang, Y., Zabludoff, A. I., & Tremonti, C. A. 2018a, The Astrophysical Journal, 862, 2

French, K. D., Zabludoff, A. I., Yoon, I., et al. 2018b, The Astrophysical Journal, 861, 123

Gao, Y., & Solomon, P. M. 2004, The Astrophysical Journal, 606, 271

Greve, T. R., Papadopoulos, P. P., Gao, Y., & Radford, S. J. E. 2009, ApJ, 692, 1432

Harris, C. R., Millman, K. J., van der Walt, S. J., et al. 2020, Nature, 585, 357

Ho, L. C., & Keto, E. 2007, ApJ, 658, 314

Hunter, J. D. 2007, Computing in Science & Engineering, 9, 90

Imanishi, M., Nakanishi, K., Kuno, N., & Kohno, K. 2004, AJ, 128, 2037

Imanishi, M., Nakanishi, K., Tamura, Y., Oi, N., & Kohno, K. 2007, AJ, 134, 2366

Jiménez-Donaire, M. J., Bigiel, F., Leroy, A. K., et al. 2019, ApJ, 880, 127

Kamenetzky, J., Privon, G. C., & Narayanan, D. 2018, ApJ, 859, 9

Kauffmann, G., Heckman, T. M., Tremonti, C., et al. 2003, MNRAS, 346, 1055

Keel, W. C., Chojnowski, S. D., Bennert, V. N., et al. 2012, MNRAS, 420, 878

Kennicutt, Robert C., J. 1998, ApJ, 498, 541

Kennicutt, Robert C., J., & De Los Reyes, M. A. C. 2021, ApJ, 908, 61

Kewley, L. J., Dopita, M. A., Sutherland, R. S., Heisler, C. A., & Trevena, J. 2001, ApJ, 556, 121

Kohno, K., Matsushita, S., Vila-Vilaró, B., et al. 2001, in Astronomical Society of the Pacific Conference Series, Vol. 249, The Central Kiloparsec of Starbursts and AGN: The La Palma Connection, ed. J. H. Knapen, J. E. Beckman, I. Shlosman, & T. J. Mahoney, 672

Krips, M., Neri, R., García-Burillo, S., et al. 2008, ApJ, 677, 262

Krips, M., Martín, S., Eckart, A., et al. 2011, ApJ, 736, 37

Law, D. R., Cherinka, B., Yan, R., et al. 2016, AJ, 152, 83

Leroy, A. K., Rosolowsky, E., Usero, A., et al. 2021, arXiv e-prints, arXiv:2109.11583

Li, Z., French, K. D., Zabludoff, A. I., & Ho, L. C. 2019, The Astrophysical Journal, 879, 131

Liu, D., Daddi, E., Schinnerer, E., et al. 2021, ApJ, 909, 56

Loenen, A. F., Spaans, M., Baan, W. A., & Meijerink, R. 2008, Astronomy and Astrophysics, 488, L5

McMullin, J. P., Waters, B., Schiebel, D., Young, W., & Golap, K. 2007, in Astronomical Society of the Pacific Conference Series, Vol. 376, Astronomical Data Analysis Software and Systems XVI, ed. R. A. Shaw, F. Hill, & D. J. Bell, 127

Meijerink, R., Spaans, M., Loenen, A. F., & van der Werf, P. P. 2011, A&A, 525, A119

Mockler, B., & Ramirez-Ruiz, E. 2021, ApJ, 906, 101

Morić, I., Smolčić, V., Kimball, A., et al. 2010, ApJ, 724, 779

Narayanan, D., & Krumholz, M. R. 2014, MNRAS, 442, 1411

Nielsen, D. M., Ridgway, S. E., De Propris, R., & Goto, T. 2012, The Astrophysical Journal, 761, L16

Papadopoulos, P. P., van der Werf, P., Xilouris, E., Isaak, K. G., & Gao, Y. 2012, The Astrophysical Journal, 751, 10

Pasha, I., Leja, J., van Dokkum, P. G., Conroy, C., & Johnson, B. D. 2020, ApJ, 898, 165

Pawlik, M. M., Wild, V., Walcher, C. J., et al. 2015, Monthly Notices of the Royal Astronomical Society, 456, 3032

Pellegrini, E. W., Smith, J. D., Wolfire, M. G., et al. 2013, ApJL, 779, L19

Privon, G. C., Herrero-Illana, R., Evans, A. S., et al. 2015, ApJ, 814, 39

Privon, G. C., Ricci, C., Aalto, S., et al. 2020, ApJ, 893, 149

Rich, J. A., Kewley, L. J., & Dopita, M. A. 2015, ApJS, 221, 28

Rowlands, K., Wild, V., Nesvadba, N., et al. 2015, Monthly Notices of the Royal Astronomical Society, 448, 258

Rowlands, K., Wild, V., Bourne, N., et al. 2018, MNRAS, 473, 1168

Sartori, L. F., Schawinski, K., Trakhtenbrot, B., et al. 2018, MNRAS, 476, L34
Sarzi, M., Shields, J. C., Schawinski, K., et al. 2010, MNRAS, 402, 2187
Sazonova, E., Alatalo, K., Rowlands, K., et al. 2021, ApJ, 919, 134
Schawinski, K., Urry, C. M., Simmons, B. D., et al. 2014, MNRAS, 440, 889
Shen, Y. 2021, arXiv e-prints, arXiv:2108.05381
Shirley, Y. L. 2015, Publications of the Astronomical Society of the Pacific, 127, 299
Smercina, A., Smith, J. D. T., Dale, D. A., et al. 2018, The Astrophysical Journal, 855, 51
Smercina, A., Smith, J.-D. T., French, K. D., et al. 2021, arXiv e-prints, arXiv:2108.03231
Snyder, G. F., Cox, T. J., Hayward, C. C., Hernquist, L., & Jonsson, P. 2011, The Astrophysical Journal, 741, 77
Stierwalt, S., Armus, L., Surace, J. A., et al. 2013, ApJS, 206, 1
Strauss, M. A., Weinberg, D. H., Lupton, R. H., et al. 2002, AJ, 124, 1810
Suess, K. A., Kriek, M., Bezanson, R., et al. 2021, arXiv e-prints, arXiv:2111.14878
Togi, A., & Smith, J. D. T. 2016, ApJ, 830, 18
Tremonti, C. A., Heckman, T. M., Kauffmann, G., et al. 2004, ApJ, 613, 898
Usero, A., Leroy, A. K., Walter, F., et al. 2015, The Astronomical Journal, Volume 150, Issue 4, article id. 115, 40 pp. (2015)., 150, arXiv:1506.00703
Valentino, F., Daddi, E., Puglisi, A., et al. 2020, A&A, 641, A155
van der Tak, F. F. S., Black, J. H., Schöier, F. L., Jansen, D. J., & van Dishoeck, E. F. 2007, A&A, 468, 627
Wang, S., & Chen, X. 2019, ApJ, 877, 116
Weiß, A., Downes, D., Neri, R., et al. 2007, A&A, 467, 955
Westfall, K. B., Cappellari, M., Bershady, M. A., et al. 2019, AJ, 158, 231
Whitaker, K. E., Kriek, M., van Dokkum, P. G., et al. 2012, The Astrophysical Journal, 745, 179
Whitcomb, C. M., Sandstrom, K., Murphy, E. J., & Linden, S. 2020, ApJ, 901, 47
Wild, V., Almaini, O., Dunlop, J., et al. 2016, Monthly Notices of the Royal Astronomical Society, 463, 832
Wild, V., Heckman, T., & Charlot, S. 2010, MNRAS, 405, 933
Wild, V., Walcher, C. J., Johansson, P. H., et al. 2009, Monthly Notices of the Royal Astronomical Society, 395, 144
Wild, V., Taj Aldeen, L., Carnall, A., et al. 2020, MNRAS, 494, 529
Yan, R., & Blanton, M. R. 2012, ApJ, 747, 61
Yun, M. S., Reddy, N. A., & Condon, J. J. 2001, ApJ, 554, 803
Zabludoff, A. I., Zaritsky, D., Lin, H., et al. 1996, The Astrophysical Journal, 466, 104

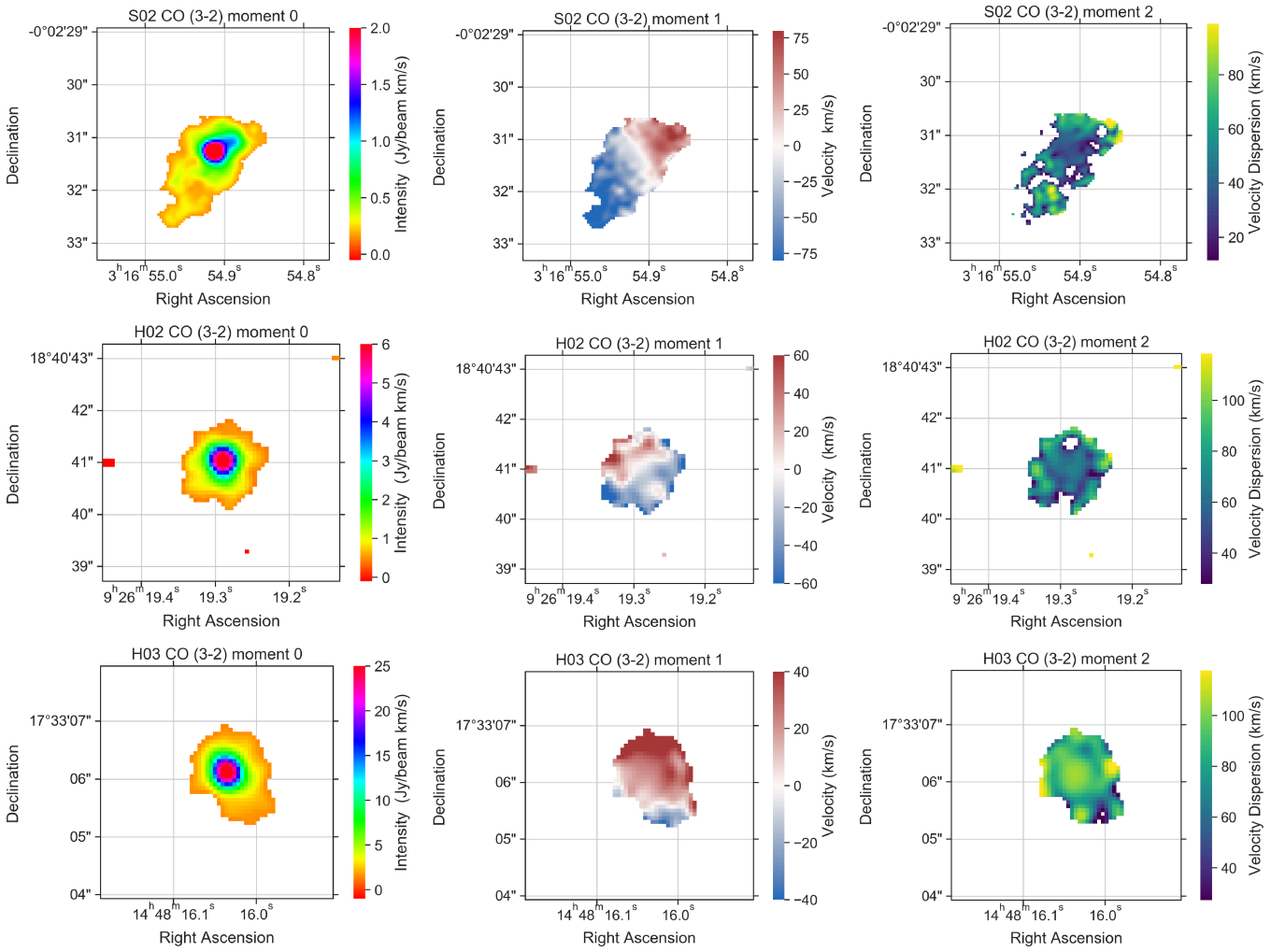

Figure 17. CO (3–2) moment maps (left column: moment 0; middle column: moment 1; right column: moment 2). Data with a signal to noise ratio of < 3 are masked. The molecular gas has limited spatial extent, with CO sizes < 1 arcsec, significantly smaller than the optical extents of the galaxies (r-band R50 values $3.72''$, $1.71''$, and $3.17''$ for S02, H02, and H03, respectively). S02 has a blueshifted component to the lower left, which we explore further in Figures 7 – 9.

APPENDIX

A. SPECTRA AND MOMENT MAPS

Moment maps for the both the CO (3–2) and HCN (1–0), HCO^+ (1–0), and HNC (1–0) datasets are shown in Figures 17 and 18. Extracted spectra are shown in Figures 19 and 20. More information can be found in §2.2.

B. INFRARED STAR FORMATION RATES

In Figures 21, 22 and 23, we consider the impact of using the TIR luminosity instead of Hα to trace the SFR in the post-starburst sample. A full comparison of the SFR tracers for this sample can be found in §4.1. Our qualitative conclusions do not change, given this sample. We observe the post-starburst galaxies to lie offset in the CO-traced gas vs. SFR plot, while they lie consistent with the comparison samples in the HCO^+ vs. SFR plot.

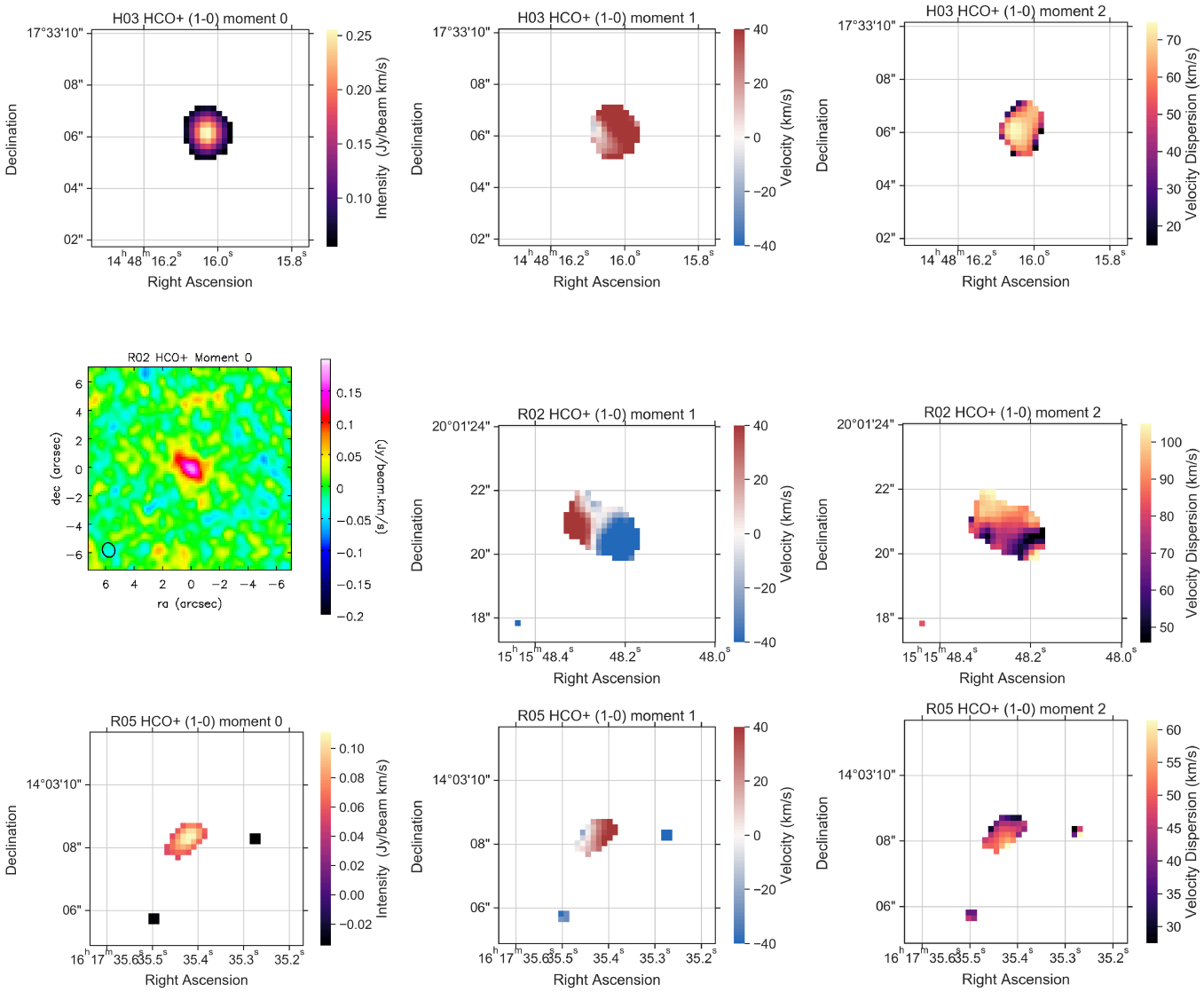

Figure 18. Moment 0 (left), moment 1(middle), and velocity dispersion (right) maps for the HCO^+ (1–0) emission for the three galaxies with detected emission.

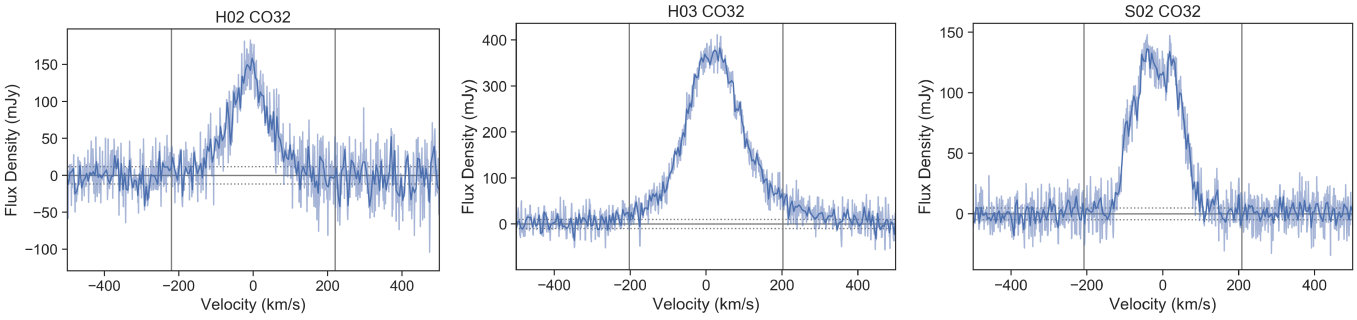

Figure 19. Extracted CO (3–2) spectra for each galaxy. For easier visualization, spectra are binned to 5 km/s (dark blue lines). A horizontal center line (grey) and uncertainty bands per 5 km/s channel (dotted grey) are added for comparison. Vertical grey lines represent the integration range for determining the total flux.

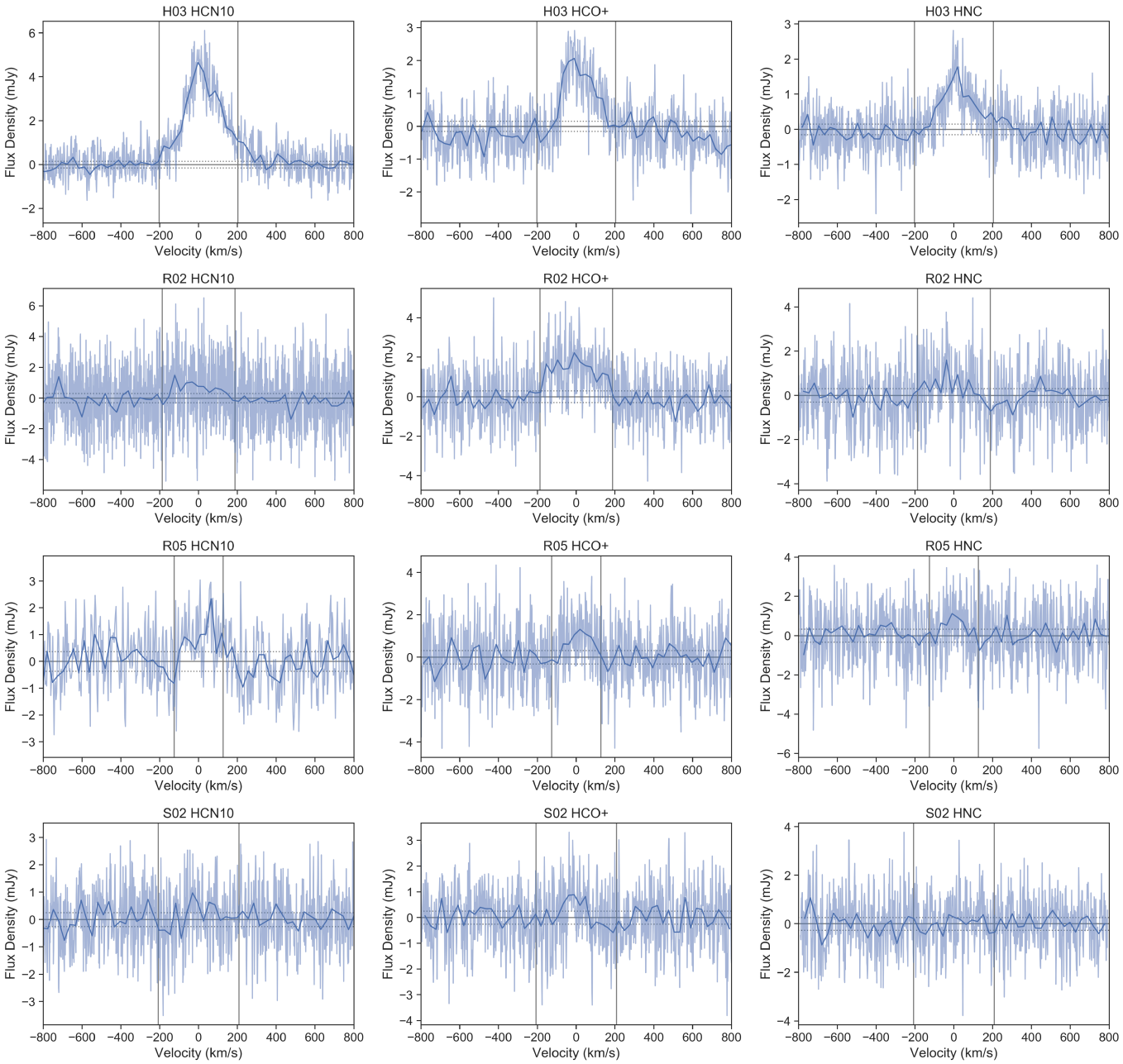

Figure 20. Extracted spectra of the three dense gas tracers (HCN (1–0), HCO^+(1–0), and HNC (1–0)) for each galaxy. For easier visualization, spectra are binned to 30 km/s (dark blue lines). A horizontal center line (grey) and uncertainty bands per 30 km/s channel (dotted grey) are added for comparison. Vertical grey lines represent the integration range for determining the total flux.

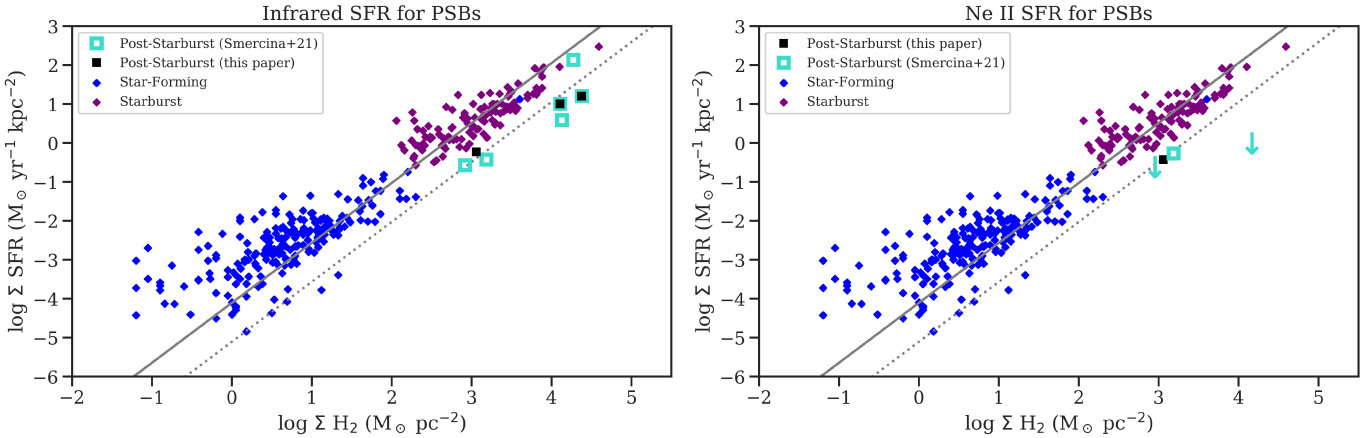

Figure 21. Same as Figure 6, but with IR-SFR indicators used instead for the post-starburst galaxy sample (left: TIR, right: [Ne II]). Molecular gas surface density vs. SFR surface density for post-starburst galaxies from this work with CO (3–2) sizes and from Smercina et al. (2021) with CO (2–1) sizes, as well as comparison samples of star-forming galaxies from de los Reyes & Kennicutt (2019) and starbursting galaxies from Kennicutt & De Los Reyes (2021). The best-fit relation from Kennicutt & De Los Reyes (2021) for the total gas density vs. star formation density is plotted in grey, with a dotted line indicating a factor of 10× below the relation. The post-starburst galaxies have very high molecular gas surface densities, yet they lie below the comparison galaxies, with low star formation rate surface densities for their molecular gas surface densities. Our qualitative conclusions here do not depend on the SFR tracer used.

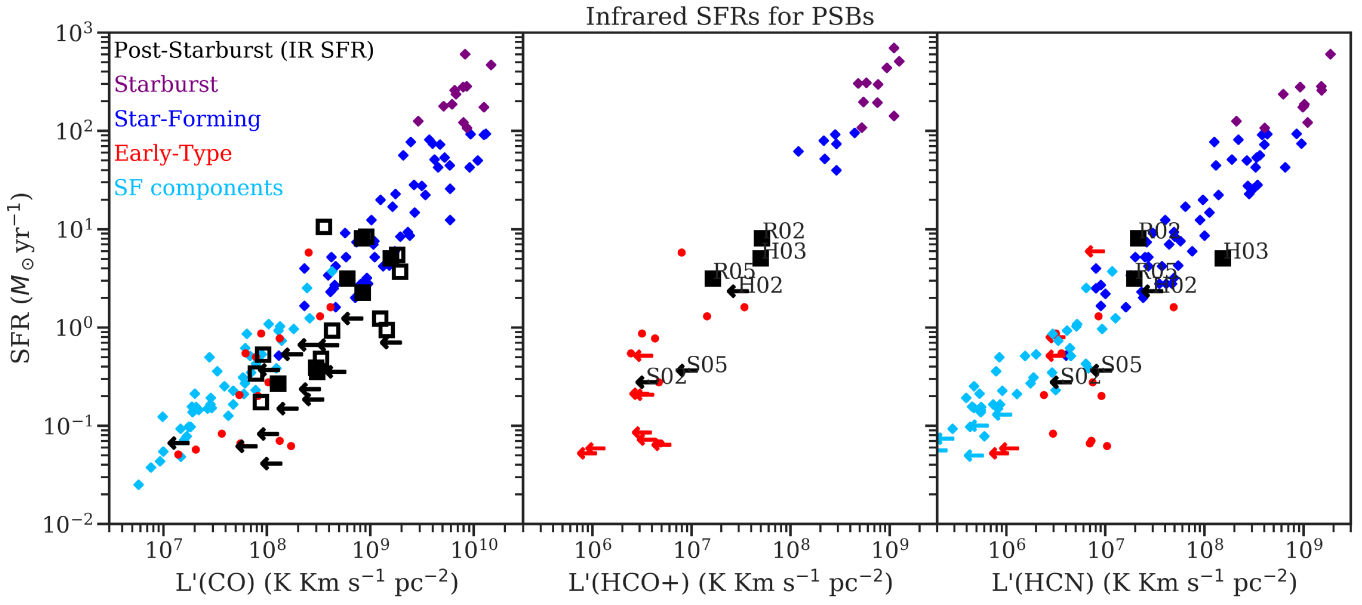

Figure 22. Same as Figure 12, but with IR-SFR indicators used instead for the post-starburst galaxy sample. (Left:) L'_{CO} vs. SFR. Early type galaxies (Crocker et al. 2012), starburst and star-forming galaxies (Gao & Solomon 2004), and star forming galaxy components (Usero et al. 2015) are correlated with low scatter, but post-starburst galaxies (French et al. 2015) have low SFRs for their CO luminosities. Black squares indicate post-starburst detections and arrows indicate 3σ upper limits. Filled squares indicate the ALMA targets considered here (including two galaxies from the Rowlands et al. (2015) sample). (Middle:) L'_{CO} vs. SFR for the same samples of galaxies. (Right:)L'_{HCN} vs. SFR for the same samples of galaxies. The post-starburst galaxies are more consistent with the comparison samples in their dense gas - star formation relations. The post-starburst galaxies have dense molecular gas properties consistent with either early type galaxies or lying between the star-forming and early type samples. Our qualitative conclusions here do not depend on the SFR tracer used.

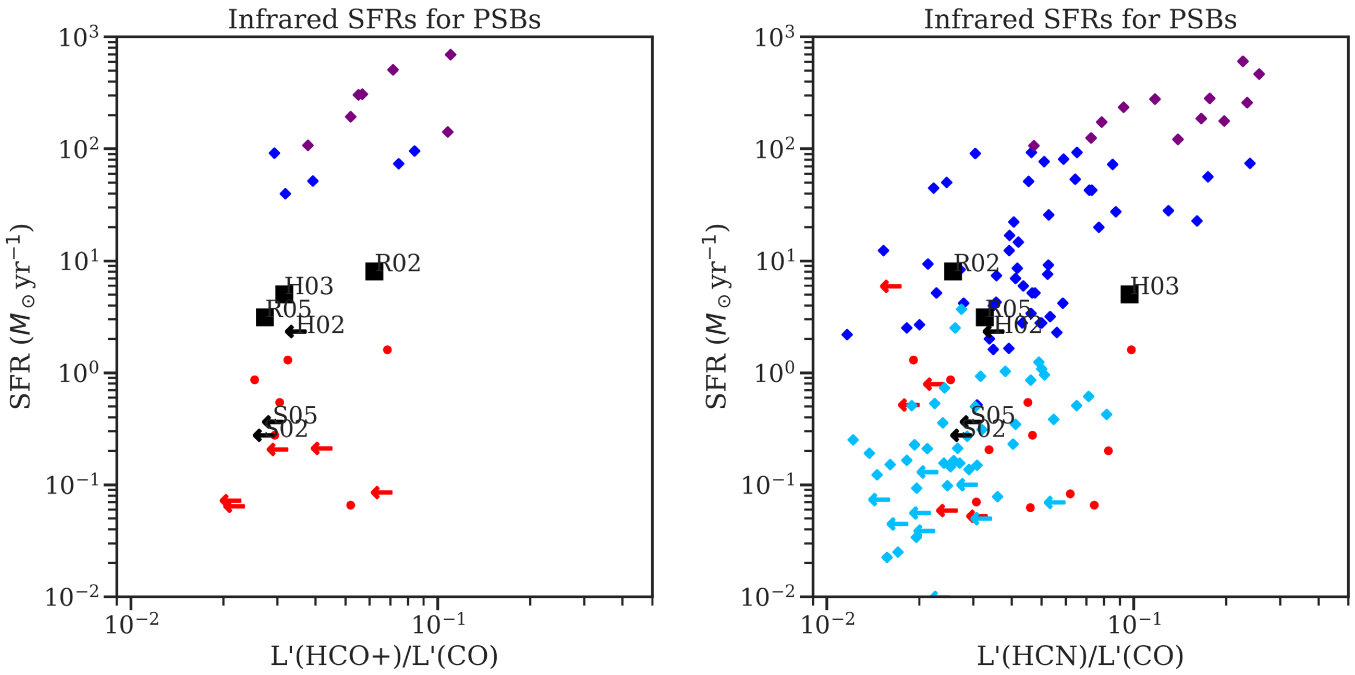

Figure 23. Same as Figure 13, but with IR-SFR indicators used instead for the post-starburst galaxy sample. (Left:) Dense gas luminosity ratio $L'_{\rm HCO+}/L'_{\rm CO}$ for the same samples as Figure 12. Post-starburst galaxies have low ratios of dense molecular gas to total molecular gas compared to other types of galaxies, although this may evolve rapidly with time during the early post-starburst phase (Figure 11). (Right:) Dense gas luminosity ratio $L'_{\rm HCN}/L'_{\rm CO}$ for the same samples. The post-starburst galaxy with high HCN/CO (H03) may have HCN luminosity increased via mechanical heating or cosmic ray heating, as it has a very high HCN/HCO+ ratio (see discussion in §3.6), and the HCN/CO ratio may overestimate the dense molecular gas fraction. Our qualitative conclusions here do not depend on the SFR tracer used.